ORIGINAL PAPER

Pressure–temperature–deformation–time path of a deformed garnet-bearing granite from the Paleoproterozoic Tandilia Belt, Río de la Plata Craton of Argentina

Melisa Angeletti[1] · Juan Cruz Martínez[1,2] · María Cristina Frisicale[1,2] · Hans-Joachim Massonne[3,4]

Abstract

The pressure–temperature (P–T) evolution of a deformed garnet-bearing granite of La Virgen hill, located 25 km south of the town of Azul, Argentina, was studied as an example of the slightly peraluminous and deformed granites widespread in the Paleoproterozoic Tandilia Belt of the Rio de la Plata Craton. An early isobaric magmatic–submagmatic cooling path followed by exhumation was derived by the appraisal of microstructures, chemical compositions of minerals and P–T pseudosection modeling in the system Si–Ti–Al–Fe–Mn–Mg–Ca–Na–K–O–H (1 wt.% of H_2O) using the software PERPLE_X. Slightly zoned magmatic garnet with a core composition of $pyr_4(grs + adr)_{11}sps_{10}alm_{75}$ equilibrated with plagioclase ($X_{An} = 0.37$) at 6.0 kbar and 655 °C in a crystal mush with < 7 vol.% of melt. The garnet rim composition of $pyr_3(grs + adr)_{12}sps_{14}alm_{71}$, texturally equilibrated with biotite (Mg/(Mg + Fe) = 0.21) at the granitic solidus of 5.9 kbar and 645 °C. The subsequent cooling path is constrained by isopleths of low-Ti muscovite with Si contents of 3.17 per formula unit commonly located around K-feldspar and recrystallized plagioclase ($X_{An} = 0.35$). Ductile deformation at low amphibolite- to greenschist-facies metamorphic conditions produced the subvertical main foliation. Forty-two chemical analyses in seven monazite grains of the granite yielded two groups of U–Th–Pb ages at 2126 ± 10 (2σ) Ma and 2089 ± 3 Ma, interpreted to be inherited from widespread magmatic events of the Tandilia Belt and resulted from the granite crystallization, respectively. The exhumation of the deformed granite from middle (~ 22 km) to upper and cold crustal levels was probably a long-lasting process after 1.9 Ga.

Keywords P–T thermodynamic modeling · Deformed garnet-bearing granite · U–Th–Pb monazite dating · Paleoproterozoic Tandilia Belt

Introduction

The earliest definitions of a geodynamic model for the evolution of the Tandilia Belt (TB) were made through lithological studies, identification of metamorphic zones, and discrimination of geochemical signatures (Teruggi et al.

1988; Ramos 1999; Ramos et al. 1990). Although modifications of these original models have been proposed, the most recent ones coincide in the suggestion of at least one continent–continent collision (Delpino and Dristas 2008; Cingolani 2011; Massonne et al. 2012; Chernicoff et al. 2014). During the last 20 years, the application of modern dating methodologies, driven by advances in isotope geochemistry, has made it possible to reliably limit the main igneous and metamorphic events of the TB to the Rhyacian until the Statherian of the Paleoproterozoic Era (*e.g.* Hartmann et al. 2002; Cingolani et al. 2002; Pankhurst et al. 2003; Cingolani et al. 2005; Rapela et al. 2007; Massonne et al. 2012; Angeletti et al. 2014; Chernicoff et al. 2015; Martínez et al. 2017, 2020; Bianchi et al. 2020). We present a study of small, slightly deformed granite body that contributes to the understanding of the geodynamics of the late collisional evolution forming the Río de la Plata Craton (RPC) in the Rhyacian.

✉ Melisa Angeletti
 melisa.angeletti@uns.edu.ar

1 Departamento de Geología, Universidad Nacional del Sur, San Juan 670, Bahía Blanca, Argentina

2 INGEOSUR-CONICET, Alem 1253, cuerpo B' 1° piso, Bahía Blanca, Argentina

3 School of Earth Sciences, China University of Geosciences, 388 Lumo Road, 430074 Wuhan, People's Republic of China

4 Fakultät Chemie, Universität Stuttgart, Pfaffenwaldring 55, 70569 Stuttgart, Germany

🍪 Springer

Our study area at La Virgen hill, located 25 km south of the town of Azul in the Buenos Aires Province, is a good example for deformed garnet-bearing granites outcropping in various places of the Tandilia Belt (TB). The granite at La Virgen hill was studied to decipher the pressure–temperature–time–deformation (*P–T–t–d*) conditions of its cooling path. For this purpose, (1) geothermobarometric modeling was applied using P–T pseudosections and their contouring with chemical parameters of interest, (2) monazite was dated 'in situ' to identify igneous-metamorphic events, and (3) microstructures were studied in rock thin sections. Our new work complements the studies (see below) of petrogenetic processes in adjacent areas within the TB. Although there are entrenched geodynamic models that explain the formation of the RPC basement through the collision of terranes (*e.g.* Oyhantçabal et al. 2018), the magnitude of the relevant collisional event and the mode of growth of the orogen during the previous accretional stage is still unknown (Massonne et al. 2012). The *P–T* conditions for the metamorphic evolution of the southeastern TB were addressed by several studies of different basements rocks (Delpino and Dristas 2008; Massonne et al. 2012; Martínez et al. 2016, 2017), whereas such studies of rocks from the northwestern part of the TB are scarce (Frisicale et al. 2005; Angeletti et al. 2017). Thus, the present work promises to be a valuable contribution to understand the evolutionary processes of the RPC basement in general.

Geological background

Regional geology of the Tandilia Belt

The TB (Fig. 1a) is the southernmost and largest exposure of the RPC, the limits of which are still debated (*e.g.* Oyhantçabal et al. 2011; Rapela et al. 2011; Santos et al. 2017). Recently, the Piedra Alta Terrane, the main RPC exposure in Uruguay, and the TB were both defined as different terranes based on their isotopic and geochemical affinities (Pamoukaghlian et al. 2017). The TB constitutes the Paleoproterozoic igneous-metamorphic Buenos Aires Complex (Marchese and Di Paola 1975) composed of granitic-tonalitic gneisses, migmatites, amphibolites, granitoids, ultramafic rocks, and subordinate schists, marbles, and felsic and mafic dikes (Fig. 1b). From the isotopic data and the geochemical signatures, these basement rocks of the TB are associated with an intra-oceanic subduction system of a primitive continental arc (Teruggi et al. 1988). The origin of these rocks included a tectonic subduction scenario (Ramos 1999) later called 'Encantadas' orogeny based on 2.2 Ma U–Pb SHRIMP zircon data (Hartmann et al. 2002). A subsequent collision during the 'Camboriu' orogeny (2.2–2.0 Ga) led to high-temperature regional metamorphism, mylonitization,

thrusting and transcurrent faulting accompanied by anatexis of the crustal rocks and the intrusion of calc-alkaline dikes during a late transtensional event (Hartmann et al. 2002). In situ monazite U–Th–Pb dating suggests a 2.13–2.14 Ga old collisional event and a profuse intrusion and crystallization of post-collisional melts at 2.01–2.07 Ga (Massonne et al. 2012; Martínez et al. 2017). Both orogenic periods shaped the Buenos Aires complex within the 'Trans-Amazonian' (Teruggi et al. 1988) or 'Transplatense' (Santos et al. 2019) orogenic cycle.

Three main structural domains with E–W, NE–SW (steeply NW-dipping axial plane foliations) and NW–SE (strike of local faults or joint planes) orientation occur in some localities of the Buenos Aires complex between the Tandil and Balcarce areas, and represent three deformational phases (Teruggi et al. 1974; Dalla Salda 1981) having been active during the Trans-Amazonian orogenic cycle. Two dike suites intruded the basement rocks of the Buenos Aires Complex. The older suite of calc-alkaline andesitic to rhyolitic composition yielded $^{40}Ar/^{39}Ar$ step-heating plateau ages of ~2.02 Ga on biotite of two baked country rocks (Teixeira et al. 2002). This suite of dikes is overprinted by low-grade metamorphism (Dristas 1983; Dristas et al. 2013; Lajoinie et al. 2014). More recently, the finding of high-pressure medium-temperature metamorphism in acidic, probably co-genetic, calc-alkaline dikes of El Quebracho hill with a crystallization age of 2.13 Ga obtained by U–Th–Pb inductively-coupled plasma (ICP) mass-spectrometry (MS) on zircon (Martínez et al. 2020) strengthens the need for more and precise dating of this igneous suite. The most important structure at a regional scale is the Azul Megashear Zone (AMSZ—Frisicale et al. 1999) which is located in the northwestern TB (Fig. 1b). The AMSZ is characterized by a lateral extent of more than 40 km, a maximum width of 2.5 km, subvertical dip and E–W strike, and mylonitization with minor cataclasis (*e.g.* Frisicale et al. 2005). The younger suite of dikes is tholeiitic and yielded U–Pb ages of ~1.6 Ga, determined by ID-thermal ionization MS on baddeleyite (Iacumin et al. 2001; Teixeira et al. 2013). In the western and southwestern areas (Fig. 1b), the Buenos Aires Complex is unconformably covered by Neoproterozoic to lower Paleozoic marine siliciclastic to carbonatic sedimentary rocks (Poiré and Spalletti 2005).

Background on the *P–T* evolution of metamorphic rocks from the Tandilia Belt

During the last years, several geothermobarometric studies on metamorphic rocks from the TB led to different *P–T* paths which can be grouped in type I = clockwise paths with cooling during exhumation (Massonne et al. 2012; Martínez et al. 2017; Bianchi et al. 2020), type II = counterclockwise paths with isobaric cooling (Delpino and Dristas 2008) or
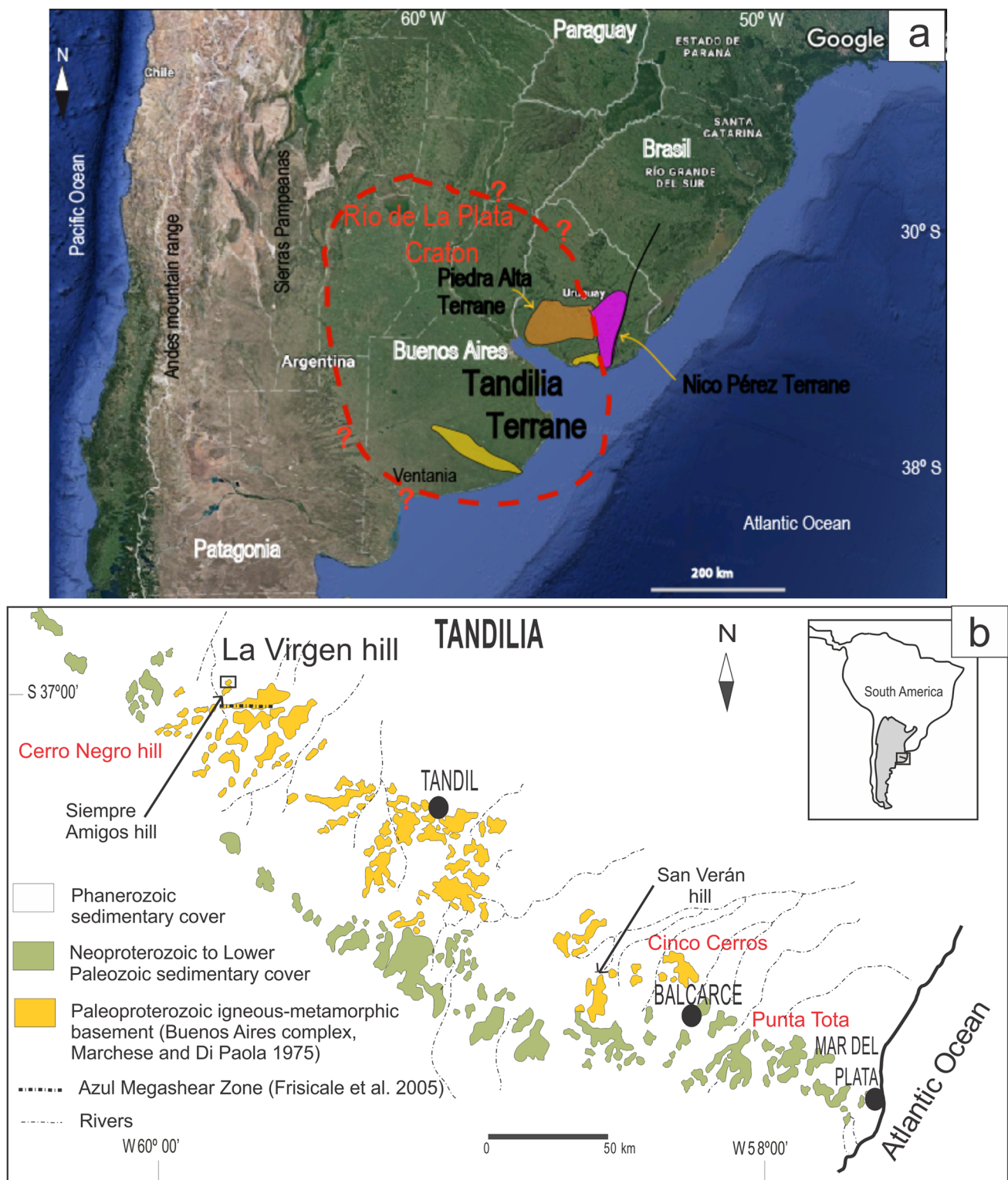
Fig. 1 **a** Regional map showing limits of the Rio de la Plata Craton, proposed by Oyhantçabal et al. (2011), and the position of the Tandilia Belt (light blue) and Piedra Alta Terrane (violet) in this craton as well as the adjacent Nico Perez Terrane (pink). **b** Geological map of the Tandilia Belt taken and modified from Hartmann et al. (2002) showing the position of La Virgen hill and other localities mentioned in the text

with increasing pressure during cooling (Martínez et al. 2016; Angeletti et al. 2017), and type III = clockwise prograde high-*P* and medium-*T* paths (Martínez et al. 2020). Type I paths were determined for high-grade metasedimentary and metagranitic rocks occurring (1) in the Cinco Cerros area (Fig. 1b), where biotite–garnet–muscovite-bearing gneiss was metamorphosed at peak *P–T* conditions of ~ 6.7 kbar at 670 ℃ (Massonne et al. 2012), (2) in San Verán hill (Fig. 1b), where migmatite and associated garnet-bearing granite experienced peak *P–T* conditions of 5.5 kbar and 630 ℃ (Martínez et al. 2017), and (3) in La Plata hill (Fig. 1b), where quartz-sillimanite nodule-bearing gneiss surpassed the melt-in curve to reach peak metamorphic conditions of ~ 680 °C at 4 kbar. Retrograde back-reactions in the presence of hydrous fluids accompanied by a syntectonic coaxial deformation event (D_1) during cooling to ~ 650 °C at 3.8 kbar generated the quartz–sillimanite nodules by K-feldspar dealkalinization (Bianchi et al. 2020).

Type II paths were determined for dolomitic marbles and associated calc-silicate rocks of the Punta Tota district (Fig. 1b) with peak *P–T* conditions of 5–6 kbar and 750–800 ℃ followed by near isobaric cooling to about 500–450 ℃ (Delpino and Dristas 2008). Amphibole-biotite gneiss from El Cristo hill (Fig. 1b) recorded increasing pressures from 8 to 12 kbar during cooling from 660 to 595 ℃ (Martínez et al. 2016). Such unusual *P–T* path was explained by the tectonic transport of rock slices from mid-crustal to deep-crustal levels along a major suture zone, at which a geothermal gradient similar to those of modern convergent margins (15 ℃km^{-1}, Martínez et al. 2016) was prevailing. A comparable path was derived for mylonitized granite from Cerro Negro hill (Fig. 1b). This rock was deformed under amphibolite-facies metamorphic conditions at 670 ℃ and 5.3 kbar, cooled down to 650 ℃ during a pressure increase to 8 kbar, and experienced an isothermal decompression to mid-crustal levels at 600 ℃ (Angeletti et al. 2017). The only type III path in the TB was derived from calc-alkaline acidic dikes of El Quebracho hill (Martínez et al. 2020). These rocks were buried during a NE–SW shortening D_1 event from 9.5 to 12 kbar accompanied by heating from 540 °C to nearly 600 °C. Afterwards, the rocks cooled down during exhumation.

Local geology of La Virgen hill

Plutonic rocks are locally exposed in the TB. These rocks were reported and studied on a regional scale by Dalla Salda et al. (2006) and Cingolani (2011). In the southeastern portion of the TB, peraluminous garnet-bearing leucogranites and associated pegmatite dikes caused by anatexis are prevalent (Teruggi et al. 1988; Delpino and Dristas 2008; Massonne et al. 2012; Martínez et al. 2016; 2017). Granitoid rocks in the northwestern portion of the TB were

geochemically classified as metaluminous to slightly peraluminous with a calc-alkaline signature (*e.g.* Pankhurst et al. 2003; Angeletti et al. 2016).

La Virgen hill is mainly constituted by one of these slightly peraluminous granitoids at the western end of the TB (Angeletti et al. 2019), located ~ 25 km south of the town of Azul and ~ 4 km north of the AMSZ (Fig. 1b). González Bonorino et al. (1956) described the situation at La Virgen hill as a 'little outcrop constituted mainly by mylonitic gray granite, with alternated dark and light layers, garnet and accessory phases as zircon and apatite showing cataclastic effects'.

General mesoscopic and microscopic features of the studied rocks

The granitoid at La Virgen hill is a globose small body exposed over an area no larger than 1.5 km^2. The dominant rock type there (Fig. 2a) is a gray garnet-bearing, deformed granite which contains bodies or layers of gray migmatite. A steeply dipping (80–90º) WNW-striking foliation (S_{1+m}) occurs in both rock types (Fig. 2b). Whitish and profuse leucocratic quartz and K-feldspar-bearing segregates are mainly concordant with S_1 and locally constitute lenses enriched in garnet grains being up to a few millimeters in diameter (Fig. 2c). These grains are either homogeneously distributed or clustered. Conspicuous thin ultramylonite zones were observed in the predominantly protomylonitic granite.

The deformed migmatite is well-foliated and composed of quartz, plagioclase, K-feldspar and biotite. Occasionally, garnet and amphibole (~ 2%) occur. Quartz with undulatory extinction, plagioclase with deformation twins (Fig. 2d) and K-feldspar with flame perthites are granoblastic with evidence of mylonitization. Myrmekitic texture was observed at recrystallized rims of K-feldspar porphyroclasts. Reddish to brown pleochroic laths of biotite define S_{1+m} (Fig. 2d). Garnet porphyroclasts as large as ~ 0.5 cm are usually poikilitic with inclusions mainly of quartz and biotite. Amphibole is rare and occurs as large crystals ranging from 0.3 to 0.5 cm and is associated with biotite, partly chloritized, and Fe oxides. Locally, more intense mylonitization led to the occurrence of ribbon mylonite (sensu stricto Passchier and Trouw 2005). Accessories in the migmatite are zircon, apatite, allanite, monazite, and Fe–Ti opaque phases.

The main minerals in the deformed granite are, in decreasing abundance, K-feldspar (orthoclase and microcline), quartz, and plagioclase, often recrystallized to a polygonal granoblastic texture. Quartz, generally with undulatory extinction, shows incipient ribbons (Fig. 3c, f) that envelope mm-sized feldspar porphyroclasts, which display deformation twins (Fig. 2d), curved twins (Fig. 3d), and flame perthites (Fig. 3b) as the more common deformation
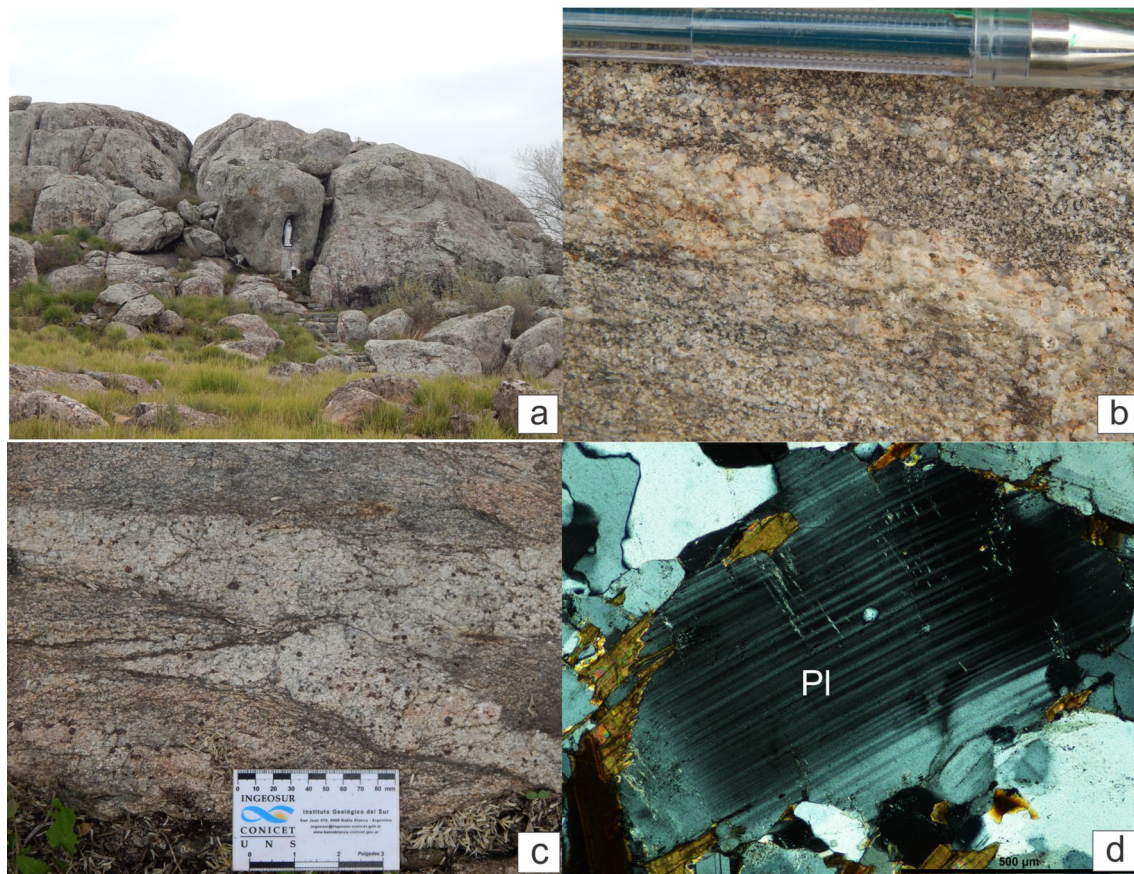
Fig. 2 Outcrop and sample photographs. **a** Outcrop at La Virgen hill. **b** Deformed garnet-bearing granite, which occasionally occurs interlayered with gray migmatite, both steeply dipping (80°–90°) with an WNW-striking main structure (S_1). **c** Whitish and profuse leucocratic quartz and K-feldspar bearing leucosomes, mainly concordant with the S_1, with lenses enriched in reddish garnet, homogeneously distributed or clustered in grains that reached few millimeters in diameter. **d** Photomicrographs (crossed polarizers) of gneiss. Plagioclase (Pl) with deformation twins as evidence of mylonitization. Laths of biotite follow the main foliation (S_1)

microstructures. Biotite, garnet, and muscovite occur in minor proportions. Garnet is easily recognized with the naked eye as reddish spots with sizes of a few millimeters in diameter. These garnet porphyroclasts (up to 5%) may show symplectitic rims with quartz and inclusions of biotite, quartz (Fig. 3c), and zircon. Biotite, partially to fully chloritized, occurs along microcracks in garnet as retrograde products. Muscovite laths show irregular shapes as replacement of feldspars or as a magmatic mineral phase with euhedral borders. Accessory phases are zircon, apatite, monazite, allanite, ilmenite, and magnetite. Fine-grained sericite is widespread replacing plagioclase.

Analytical and calculation methods

Chemistry of main minerals and bulk-rock

Petrographic observations and descriptions are based on inspection of thin sections under the polarizing microscope on several samples of garnet-bearing deformed granite of La Virgen hill. We selected sample LV0604 as a representative one of the deformed granite. The chemistry of minerals in this sample was examined at the former *Institut für Mineralogie und Kristallchemie, Universität Stuttgart* (Germany), using a CAMECA SX100 electron microprobe (EMP) equipped with five wavelength-dispersive spectrometers. Full quantitative analyses of plagioclase, K-feldspar (Table 1), muscovite, biotite (Table 2), and garnet (Table 3) were conducted with the operating conditions of 10 nA for beam current, 15 kV for the acceleration voltage, and a beam diameter of *ca.* 3 µm. The concentrations of Na, K, Ti, Mg, Mn, Fe, Ca, Si, Al, and Cr (garnet) or Ba (other minerals) were determined. For Ti, Cr, and Ba (PET) and Fe and Mn (LiF) measurements large spectrometer crystals were used. Standards were natural minerals (wollastonite for Si and Ca Kα1-radiation, rutile for TiKα1, rhodonite for MnKα1, orthoclase for K Kα1, albite for Na Kα, periclase for Mg Kα1), pure Fe_2O_3 and Cr_2O_3 for FeKα$_1$ and CrKα$_1$, respectively, and
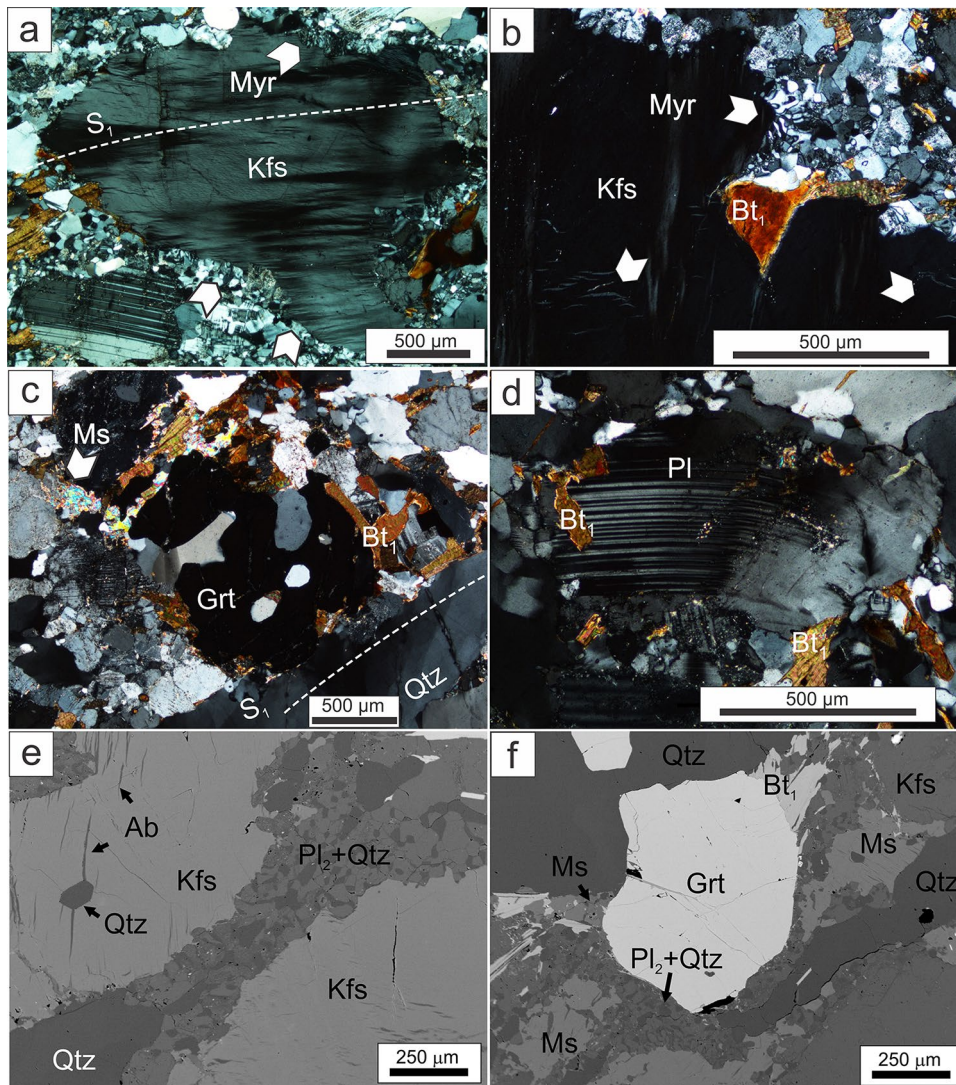
Fig. 3 Photomicrographs (crossed polarizers) of the studied deformed garnet-bearing granite. **a** Large porphyroclasts of K-feldspar (Kfs) and plagioclase (Pl) with their longer axes parallel to the S_1 foliation and a thin mantle of grains formed by progressive recrystallization (white arrow). Myrmekite colonies (Myr) developed at plagioclase and K-feldspar grain boundaries. **b** Another large porphyroclast of K-feldspar. White arrows point to flame perthites and mymekitic texture (Myr). Large biotite laths (Bt_1) differ from recrystallized biotite in the matrix. **c** Garnet (Grt) porphyroclasts are poikilitic and xenomorphic with rounded shapes. Some of the microstructures developed by crystal-plastic deformation in quartz (Qtz) leading to rare incipient oriented ribbons (S_1). Muscovite laths (Ms) grew outside garnet crystals. **d** Plagioclase (Pl) shows bent deformation twins. Biotite laths are usually bent and altered to chlorite and envelope feldspar porphyroclasts. **e** Back-scattered electron (BSE) image. The fine-grained recrystallized plagioclase and quartz ($Pl_2 + Qtz$) in a core-and-mantle texture around perthitic K-feldspar (Kfs) porphyroclasts point to deformation during exhumation of the granite. Quartz (Qtz) occurs as inclusion in a K-feldspar (Kfs) porphyroclast. **f** BSE images showing large and anhedral muscovite laths commonly appear at K-feldspar margins. Garnet (Grt) porphyroclast is surrounded by incipient Qtz ribbons, biotite (Bt_1) laths that grew outside garnet, and fine-grained recrystallized plagioclase and quartz ($Pl_2 + Qtz$)

Ba glass for $BaL\alpha_1$. The PaP correction procedure provided by CAMECA was applied. The structural formulae of minerals were calculated with the CALCMIN software (Brandelik 2009). Results on representative analyses of the main minerals are presented in Tables 1, 2, and 3. X-ray scanning maps of Ca, Fe, Mn, and Mg for garnet porphyroclasts were produced by stepwise movement (every 100 or 200 ms) of the thin section under the electron beam

(50 nA) of the microprobe and subsequent computer-aided evaluation.

The bulk-rock analysis of the selected sample (Table 4) was achieved at Bureau Veritas Acme Labs, Chile, with rock powder (85% passing 200 mesh) obtained by grinding this sample. A glass disk, prepared from this powder + Spectromelt, was analyzed with X-ray fluorescence for major elements. After fusion of rock powder with lithium borate and

Table 1 Representative electron microprobe analyses (oxides in wt.%) of feldspars in the garnet-bearing metagranite (LV0604)

Mineral	Pl$_1$				Pl$_2$			K-feldspar					
Analysis n^o	#24	#26	#27	#28	#80	#81	#83	#35	#36	#37	#38	#39	#85
SiO$_2$	58.97	59.06	59.08	59.08	59.73	59.86	59.88	64.82	64.69	64.82	64.59	64.79	64.60
Al$_2$O$_3$	26.31	26.30	26.49	26.23	26.01	26.00	25.86	18.60	18.56	18.39	18.73	18.56	18.64
Fe$_2$O$_3$	0.28	0.23	0.19	0.13	0.05	0.00	0.00	0.18	0.21	0.23	0.23	0.17	0.00
CaO	7.94	7.99	8.07	8.14	7.58	7.55	7.18	0.01	0.14	0.01	0.01	0.01	0.06
Na$_2$O	7.21	7.17	7.20	7.12	7.42	7.52	7.40	0.52	0.52	0.62	0.68	0.62	1.22
K$_2$O	0.13	0.16	0.13	0.16	0.13	0.10	0.17	16.61	16.77	16.69	16.88	16.61	15.68
BaO	0.00	0.00	0.02	0.00	0.00	0.00	0.00	0.53	0.46	0.51	052	0.51	0.59
Sum (cor.)	100.87	100.95	101.23	100.89	100.95	101.03	100.52	101.30	101.37	101.29	101.67	101.29	100.99
Cations	Normalization on the basis of 16 negative charges												
Si	2.615	2.617	2.611	2.620	2.640	2.644	2.654	2.979	2.975	2.982	2.966	2.979	2.971
Al	1.375	1.374	1.380	1.371	1.355	1.353	1.351	1.008	1.006	0.997	1.014	1.005	1.019
Fe^{3+}	0.009	0.007	0.006	0.004	0.000	0.000	0.000	0.006	0.007	0.008	0.008	0.006	0.000
Ca	0.377	0.379	0.382	0.387	0.359	0.357	0.341	0.001	0.007	0.000	0.001	0.000	0.001
Na	0.620	0.616	0.617	0.612	0.636	0.644	0.635	0.047	0.047	0.055	0.060	0.055	0.109
K	0.007	0.009	0.007	0.009	0.007	0.006	0.009	0.974	0.984	0.979	0.989	0.974	0.920
Ba	0.000	0.000	0.000	0.000	0.000	0.000	0.000	0.010	0.008	0.009	0.009	0.009	0.011
X$_{An}$	0.376	0.378	0.380	0.384	0.358	0.355	0.346	0.010	0.014	0.009	0.009	0.009	0.013
X$_{Ab}$	0.617	0.613	0.612	0.607	0.634	0.639	0.644	0.045	0.044	0.053	0.057	0.053	0.104
X$_{Or}$	0.007	0.009	0.008	0.009	0.007	0.005	0.010	0.945	0.941	0.938	0.933	0.938	0.883

Pl$_1$ porphyroclast, *Pl$_2$* recrystallized plagioclase

digestion in diluted nitric acid ICP optical emission spectrometry was used for analyzing minor and trace elements. The lower detection limit for all major elements was 0.01 wt.% (related to oxides) except for Fe (0.04 wt.%).

P–T pseudosection modeling

The bulk-rock composition, obtained at Bureau Veritas Acme Labs, was simplified to the 11-component system Si–Ti–Al–Fe–Mn–Mg–Ca-Na–K–O–H and used (Table 4) for the construction of a *P–T* pseudosection in the range of 1.0–8.2 kbar and 450–800 ℃ based on the minimum Gibbs energy algorithm of the PERPLE_X software package (Connolly 1990—version downloaded in August 2011 from http://www.perplex.ethz.ch). The pseudosection calculations were undertaken with the internally consistent thermodynamic dataset by Holland and Powell (1998, updated in 2002) for end-member minerals and the equation of state for H$_2$O (model *CORK*: Holland and Powell 1991). We applied solid-solution models documented in *newest_format_solut.dat* in PERPLE_X (Massonne et al. 2018) and compatible with the thermodynamic data set: *Chl*(HP) for chlorite, *Ep*(HP) for clinozoisite-epidote, *Cpx*(HP) for clinopyroxene, *Opx*(HP) for orthopyroxene, and *Gt*(HP) for garnet published by Holland and Powell (1998), *TiBio*(HP) for biotite (Powell and Holland 1999),

and *Amph*(DHP) for amphibole (Dale et al. 2000). Models *Pheng*(HP) for potassic white mica, *Ctd*(HP) for chloritoid, and *St*(HP) for staurolite were selected from "THERMOCALC" (*written com.* by J.A.D. Connolly). For plagioclase and K-feldspar the model by Fuhrman and Lindsley (1988) was applied, but for practical reasons (see Massonne 2010) subdivided into *fsp11* (limit: 10 mol.% K-feldspar) and *fsp21* (80 mol.% albite + 3 mol.% anorthite). The ideal solutions *hCrd* (for Fe^{2+}-Mg-Mn^{2+}-cordierite with variable water contents) and *IlGkPy* (for ilmenite-geikilite-pyrophanite) were used, which are based on the thermodynamic data for the corresponding end-members given by Holland and Powell (1998). Furthermore, *Usp*(M) for magnetite-ulvöspinel (Massonne 2011), and *melt*(HP) to model the formation of haplogranitic melt (White et al. 2003) were selected. The pseudosection was calculated considering a relevant O$_2$ content taking 7% of Fe being trivalent into account (see, Massonne 2012). A content of 1 wt.% of H$_2$O for the granite was assumed to assure water-saturated conditions at the super-solidus state near the solidus (Massonne et al. 2012). After setting the O$_2$ and H$_2$O contents, the bulk-rock composition was normalized to 100% (Table 4). The contouring of the *P–T* pseudosection was achieved through diagrams presenting the variation of chemical parameters in garnet, muscovite and plagioclase with the subprograms *werami.exe* and

Table 2 Representative electron microprobe analyses (oxides in wt.%) of biotite and K-white mica (Ms_1 and Ms_2) the garnet-bearing metagranite (LV0604)

Mineral	Biotite			Ms_1	Ms_2		
Analysis n^o	#60	#61	#63	#57	#54	#55	#56
SiO_2	34.62	34.58	34.61	45.51	46.33	45.95	46.851
TiO_2	3.88	3.73	3.77	0.53	0.17	0.18	0.12
Al_2O_3	17.29	16.95	17.19	32.31	32.23	32.73	32.18
Fe_2O_3	0.00	0.00	0.00	0.71	0.00	0.50	0.00
FeO	26.08	26.14	25.81	3.48	3.75	3.49	3.55
MnO	0.06	0.09	0.07	0.05	0.00	0.01	0.00
MgO	3.93	4.03	3.95	0.90	0.90	0.82	0.89
CaO	0.03	0.00	0.02	0.02	0.00	0.00	0.00
Na_2O	0.09	0.04	0.06	0.25	0.21	0.17	0.21
K_2O	9.86	10.10	9.76	11.57	11.69	11.70	11.51
BaO	0.31	0.28	0.26	0.58	0.21	0.19	0.143
H_2O (calc.)	3.814	3.797	3.79	4.40	4.41	4.42	4.43
Sum (cor.)	99.98	99.74	99.31	100.328	99.92	100.10	99.866
Cations	Normalization on the basis of 22 negative charges. all Fe as Fe^{2+}			Fe^{2+}–Fe^{+3} calculation; $42 - (Ca + Ba)$ valencies			
Si	2.722	2.731	2.734	6.199	6.302	6.234	6.3455
Al^{IV}	1.278	1.269	1.266	1.801	1.697	1.766	1.6545
Sum_T	4.000	4.000	4.000	8.000	8.000	8.000	8.0000
Ti	0.230	0.222	0.224	0.054	0.017	0.019	0.0119
Al^{VI}	0.324	0.309	0.335	3.386	3.470	3.468	3.4821
Fe^{2+}	1.714	1.726	1.705	0.397	0.427	0.396	0.4016
Mn	0.004	0.006	0.005	0.006	0.000	0.001	0.0000
Mg	0.461	0.475	0.466	0.183	0.183	0.165	0.1788
Sum_R	2.733	2.738	2.735	4.100	4.097	4.100	4.0743
Ca	0.003	0.000	0.002	0.003	0.000	0.000	0.0000
Na	0.014	0.006	0.009	0.07	0.056	0.045	0.0545
K	0.989	1.017	0.984	2.010	2.029	2.024	1.988
Ba	0.010	0.009	0.008	0.031	0.0115	0.010	0.01
Sum_A	1.015	1.032	1.003	2.111	2.096	2.080	2.050
H	2.000	2.000	2.000	4.000	4.000	4.000	4.000
Mg#	0.21	0.22	0.21				
X_{Ms}				0.742	0.754	0.779	0.750

pscontor.exe. All raw graphics generated with *psvdraw.exe* and *pscontor.exe* were smoothed and redrawn according to Connolly (2005).

Monazite dating

Fifty-four in situ U–Th–Pb ages of monazite in two lead-free polished thin sections of sample LV0604 were obtained with the wavelength-dispersive system of the aforementioned EMP (Table 5). The analytical conditions were a spot size of *ca.* 5 μm, 180 nA beam current, and 20 kV acceleration voltage. We analyzed the concentration of Si, P, S, Ca, Y, Pb, U, Th, and light to medium REEs in monazite using the following emission lines (natural and synthetic standards, and counting times on peak and background each are given in parentheses): Si Kα (wollastonite, 200 s), P Kα (La-phosphate, 20 s), S Kα (barite, 50 s), Ca Kα (wollastonite, 20 s), Y Lα (Y-phosphate, 200 s), La Lα (La-phosphate, 50 s), Ce Lα (Ce-phosphate, 20 s), Pr Lβ (Pr-phosphate, 40 s), Nd Lβ (Nd-phosphate, 100 s), Sm Lβ (Sm-phosphate, 250 s), Gd Lβ (Gd-phosphate, 50 s), Dy Lβ (Dy-phosphate, 200 s), Pb Mα (crocoite, 500 s) using a large PET spectrometer crystal, Th Mα (thorite, 120 s) and U Mβ (uraninite, 230 s). Oxygen was stoichiometrically calculated. Corrections for U Mβ and Pb Mα

Table 3 Representative electron microprobe analyses (oxides in wt.%) of garnet in the garnet-bearing metagranite LV0604

Mineral	Garnet core				Garnet rim			
Analysis n^o	Grt1#20	Grt1#17	Grt1#15	Grt2#49	Grt1#6	Grt1#1	Grt1#2	Grt2#34
SiO_2	37.04	37.02	37.14	36.73	36.99	36.94	37.05	37.02
TiO_2	0.00	0.02	0.00	0.01	0.01	0.00	0.01	0.00
Al_2O_3	20.72	20.69	20.75	20.90	20.62	20.58	20.71	20.67
Fe_2O_3	0.20	0.06	0.00	0.00	0.13	0.05	0.00	0.16
FeO	32.60	32.70	32.51	32.95	31.87	31.20	31.55	32.77
MnO	4.45	4.28	4.47	4.45	5.14	5.93	5.46	5.05
MgO	1.05	0.99	0.93	0.91	0.84	0.68	0.69	0.59
CaO	3.94	3.90	4.01	3.83	3.99	4.00	4.08	3.86
Na_2O	0.03	0.00	0.00	0.00	0.03	0.01	0.00	0.00
Sum (corr.)	100.07	99.69	99.84	99.81	99.67	99.43	99.60	100.18
Cations	Normalization on the basis of 48 negative charges. 10 six- and eight-fold coordinate cations							
Si	6.026	6.060	6.074	5.977	6.060	6.078	6.088	6.046
Ti	0.000	0.002	0.000	0.001	0.001	0.000	0.002	0.001
Al	3.973	3.992	4.000	4.008	3.982	3.992	4.012	3.978
Fe^{3+}	0.024	0.007	0.000	0.000	0.016	0.007	0.000	0.020
Fe^{2+}	4.434	4.476	4.447	4.484	4.366	4.293	4.336	4.476
Mg	0.256	0.242	0.228	0.222	0.206	0.168	0.170	0.144
Ca	0.687	0.683	0.702	0.668	0.701	0.706	0.718	0.676
Mn	0.613	0.593	0.619	0.614	0.714	0.827	0.761	0.699
Na	0.009	0.003	0.000	0.001	0.011	0.005	0.000	0.003
X_{Ca}	0.11	0.114	0.117	0.111	0.116	0.117	0.120	0.112
X_{Mg}	0.04	0.040	0.038	0.037	0.034	0.028	0.028	0.024
X_{Mn}	0.10	0.098	0.103	0.102	0.119	0.137	0.127	0.116
X_{Fe}	0.73	0.746	0.741	0.748	0.727	0.715	0.724	0.746

were applied for interferences with the lines of Th Mγ, and with Th and Y, respectively (Massonne et al. 2012 and references therein). Measurements of lanthanides were achieved with LIF (La, Ce, Nd, Sm) and large LIF (Pr, Gd, Dy) spectrometer crystals. For the background measurements of these elements, recommendations by Reed and Buckley (1998) were followed. The analytical procedure was tested as indicated in Massonne et al. (2012) against Early Ordovician monazite from Brazil (Massonne et al. 2007) and Late Tertiary monazite from the Himalayas (Liu et al. 2011) which had been also dated with a SHRIMP and a TIMS, respectively. Reproducibility of the determined ages guarantees that the here presented ages are precise within the 1σ-error calculated for every single analysis. Chemical formulae, ages, and errors were computed with the MINCALC-V5 software (Bernhardt 2007). After clustering different populations of monazite based on their geochemical features, the statistical treatment of the obtained U–Th–Pb ages and their associated errors (1σ) was undertaken with the IsoplotR software (Vermeesch 2018) to obtain weighted mean ages.

Results

Microscopy and mineral chemistry of the garnet-bearing, deformed granite

The analyzed rock is composed of K-feldspar (37 vol.%), quartz (30 vol.%), plagioclase (18 vol.%), biotite (7 vol.%), garnet (5 vol.%), muscovite (2 vol.%), and zircon, apatite, monazite, allanite, ilmenite, and magnetite as accessory phases (1 vol.%). The porphyroclastic texture is characterized by 15 vol.% of a fine-grained (20–100 μm) granoblastic matrix (Fig. 3a). Large porphyroclasts are mainly K-feldspar (> 100 μm) and plagioclase, with their long axes parallel to the $S_1 + m$ foliation. K-feldspar shows a thin mantle of recrystallized grains by progressive recrystallization (Fig. 3a). Orthoclase shows flame perthite and graphic texture (Fig. 3b). Albite contents in K-feldspar porphyroclasts range from 4 to 10 mol.% (Table 1). Microstructures developed by crystal-plastic deformation in quartz are undulatory extinction, deformation lamellae and rare underdeveloped ribbons (Fig. 3c). Polygonal granoblastic texture of quartz formed by recrystallization

Table 4 Bulk-rock compositions (in wt.%) of the Grt-bearing metagranite (Sample LV0604)

Rock type	Grt-bearing meta-granite	
Sample n^o	LV0604	LV0604*
SiO_2	68.38	68.63
TiO_2	0.27	0.27
Al_2O_3	16.33	16.39
Fe_2O_3	2.98	
FeO		2.69
O_2		0.02
MnO	0.04	0.04
MgO	0.31	0.31
CaO	2.94	2.87
Na_2O	2.93	2.94
K_2O	4.82	4.84
P_2O_5	0.06	
LOI	0.50	
H_2O		1.00
Sum	99.26	100.00

The simplified compositions (*) to the 11-components system Na–Ca–K–Fe–Mn–Mg–Al–Si–Ti–H–O were used for the PERPLE_X calculations of bulk-rock

caused by subgrain rotation and grain boundary migration. Plagioclase present as porphyroclasts (Pl_1) is andesine with 37–38 mol.% anorthite component (Table 1), shows deformation polysynthetic twins (Fig. 3d), and is recrystallized (Pl_2) to myrmekite colonies (Fig. 3a, e). Pl_2 is slightly poorer in anorthite component (35–36 mol.%) than Pl_1 (Table 1). Feldspar shows incipient replacement by secondary muscovite, sericite and rare epidote.

Biotite laths (Bt_1) are usually bent, rarely altered to chlorite, and surround feldspar and garnet porphyroclasts with a preferred orientation subparallel to S_{1+m} (Fig. 3c, d, f). Bt1 is characterized by Mg# ($= Mg/(Mg + Fe)$) values between 0.21 and 0.22, Si contents between 2.72 and 2.73 per formula unit (pfu), low MnO, ranging from 0.06 to 0.09 wt.%, and TiO_2 contents around 4 wt.% (Table 2). In the ternary plot $10*TiO_2$-(FeO + MnO)-MgO after Nachit et al. (2005) the trend of Bt_1 compositions falls into the magmatic field (Fig. 4a). Large and anhedral muscovite laths commonly at K-feldspar borders (Fig. 3f) show slightly variable compositions with Si = 3.09–3.17 pfu, TiO_2 contents between 0.1 and 0.5 wt.%, and 74–76 mol.% of muscovite component (Table 2). In the ternary plot TiO_2–FeO*-MgO by Monier et al. (1984), these muscovite compositions plot in the field of primary (Ms_1) and late to post-magmatic muscovite Ms_2 (Fig. 4b). If so, the relatively large mica laths crystallized first as a late magmatic phase (Ms1) from a Ti-bearing magma and grew

further (Ms2) replacing feldspar at subsolidus conditions (see Massonne et al. 2012).

Garnet porphyroclasts are poikilitic and xenomorphic; some grains are rounded (Fig. 3c) and others show elongated shapes, with their long axes oriented along S_{1+m}. The composition of garnet is rather homogeneous as can be noticed in the scanned X-ray element maps (Fig. 5). Towards the rim, Ca and Mn contents in the almandine-rich garnet slightly increase (spessartine component from 10 to 14 mol.%), whereas the Mg contents decrease from 4 to 3 mol.% pyrope component (Fig. 6). Although the grossular (+ andradite) content remains almost constant at 11 mol.%, a very small increment is recorded rimward with 12 mol.% of grossular component. Late biotite (Bt_2) crystals, partially altered to chlorite and rare secondary xenomorphic Ms_2, occur in cracks within garnet porphyroclasts (Figs. 3c and 4b). Not all compositions of different types of Bt_2 and Ms_2 such as sericite were determined.

P–T pseudosection modeling and evolution path

The P–T pseudosection calculated for sample LV0604 is presented in Fig. 7. For the selected 1 wt.% of H_2O, the P–T position of the solidus curve is located at the lowest temperature of 630 °C at about 8 kbar. At 1 kbar the solidus temperature is 740 °C. Quartz, K-feldspar and plagioclase are omnipresent within the selected P–T frame. Amphibole and epidote occur only in a zone of high P/T ratios. The stability of muscovite in the modeled P–T frame is limited by the K-white mica-in curve, which intersects the solidus at 660 °C and 4.0 kbar. For super-solidus conditions, the K-white mica-in curve extends to 730 °C at the upper-pressure limit of the P–T diagram. The biotite-in curve has a similar dP/dT slope as the K-white mica-in curve but at 100 °C higher temperatures. As the granite is peraluminous (ASI = 1.07), the Al_2SiO_5 polymorphs sillimanite and andalusite appear in a low-pressure (< 4.0 kbar) narrow field with lower and higher temperature limits given by the solidus and the K-white mica-in curve, respectively. Cordierite occurs at temperatures higher than 570 °C and pressures lower than 2.8 kbar. Clinopyroxene and orthopyroxene are also stable in small fields at high pressure (> 7.0 kbar, fields 1 and 2) and low pressure (< 4.5 kbar and > 700 °C), respectively. Garnet is stable in a wide P–T range except for the low P and T zone and for pressures < 6.0 kbar and temperatures < 620 °C (Fig. 7).

Contouring of the pseudosection by chemical parameters of minerals (molar components in garnet, Si pfu in muscovite, Mg# in biotite, and anorthite in plagioclase) and volume (%) of melt and biotite is presented in Fig. 8a–c. The initial P–T conditions derivable for sample LV0604 are constrained by the intersection of isopleths for molar fractions of garnet components (Fig. 9a). The

Table 5 Representative EMP analyses of monazite in the garnet-bearing metagranite LV0604 (see Supplementary Table 1)

Analysis n^o	Mnz4#11	Mnz4#14	Mnz5# 21	Mnz5#24	Mnz6#27	Mnz6#30	Mnz7#34
SiO_2 in wt.%	0.74	0.80	0.73	0.79	0.77	0.78	0.64
P_2O_5	27.95	28.16	28.03	27.74	27.75	27.57	28.12
As_2O_5	0.00	0.01	0.00	0.02	0.01	0.00	0.00
CaO	0.72	0.59	0.62	0.65	0.62	0.58	0.55
Y_2O_3	1.00	0.27	0.52	0.48	0.37	0.37	0.86
La_2O_3	13.00	13.27	13.44	13.01	13.48	13.47	13.80
Ce_2O_3	29.20	30.19	30.06	29.60	30.08	30.16	29.82
Pr_2O_3	3.23	3.36	3.27	3.26	3.28	3.32	3.22
Nd_2O_3	11.90	12.45	11.97	12.22	12.18	12.28	11.91
Sm_2O_3	1.95	1.93	2.00	2.01	1.89	1.90	1.90
Gd_2O_3	1.28	1.05	1.20	1.18	1.05	1.05	1.21
Dy_2O_3	0.43	0.21	0.34	0.31	0.26	0.25	0.36
PbO	0.56	0.51	0.51	0.54	0.49	0.48	0.42
ThO_2	4.48	4.23	4.34	4.71	4.58	4.33	3.43
UO_2	0.40	0.34	0.31	0.30	0.23	0.21	0.28
Total oxides	96.86	97.36	97.35	96.81	97.06	96.75	96.55
Cations	Based on 4 oxygens						
Si	0.030	0.032	0.029	0.032	0.031	0.032	0.026
P	0.967	0.969	0.968	0.964	0.963	0.962	0.973
Ca	0.031	0.025	0.027	0.028	0.027	0.025	0.024
Y	0.021	0.005	0.011	0.010	0.008	0.008	0.018
La	0.196	0.199	0.202	0.197	0.204	0.204	0.208
Ce	0.437	0.449	0.449	0.445	0.451	0.455	0.446
Pr	0.048	0.049	0.048	0.048	0.049	0.049	0.048
Nd	0.173	0.181	0.174	0.179	0.178	0.180	0.174
Sm	0.027	0.027	0.028	0.028	0.026	0.027	0.026
Gd	0.017	0.014	0.016	0.016	0.014	0.014	0.016
Dy	0.005	0.002	0.004	0.004	0.003	0.003	0.004
Pb	0.006	0.005	0.005	0.006	0.005	0.005	0.004
Th	0.041	0.039	0.040	0.044	0.042	0.040	0.032
U	0.003	0.003	0.002	0.002	0.002	0.001	0.002
Cation sum	2.008	2.005	2.007	2.008	2.009	2.010	2.006
Age (Ma)	2121.67	2092.34	2104.92	2091.82	2045.42	2114.72	2135.67
1σ (Ma)	18.23	18.88	18.98	18.17	18.46	19.73	22.06

garnet core composition $pyr_4(grs + adr)_{11}sps_{10}alm_{75}$, which equilibrated with andesine (37 mol.% of anorthite), yields suprasolidus P–T conditions of 6.0 kbar and 655 °C (point A in Fig. 9a). Before reaching point A by cooling, the crystal mush crossed the muscovite-in curve at ~ 30 °C higher temperatures resulting in crystallization of Ms_1 with Si content of 3.10 pfu and a more calcic andesine with 38 mol.% of anorthite (Fig. 8b). The stable mineral assemblage at these initial conditions is quartz + plagioclase + K-feldspar + biotite + muscovite + garnet + ilmenite + magnetite-ulvöspinel, as observed in the natural rock (plus a decreasing volume of melt from 10 to 7 vol%, Fig. 9b). The minor compositional change in garnet

towards its rim leads to slightly decreasing P–T conditions to 5.9 kbar and 645 °C. Although the *P–T* conditions for the formation of the garnet core and rim are within an estimated error of ± 0.2 kbar and 30 °C for the applied methodology (see Massonne 2012), this short path is compatible with the cooling of a pluton. The garnet rim composition is texturally equilibrated with biotite (Figs. 3c and 5b), which is supported by the crosscut of the Mg# isopleth of 0.21 in Bt_1 at the disappearance of melt at point B (Fig. 9b). The calculated mineral mode of garnet at the solidus is lower (0.4 vol.%) than the maximal observed amount (5 vol.%) probably due to clustering observed in the rock. The subsequent cooling (see discussion) path is
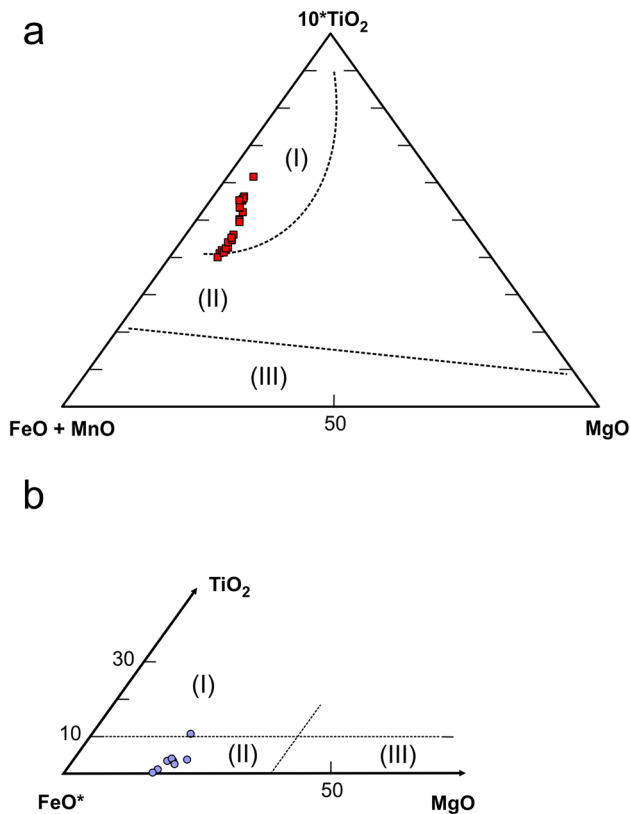
Fig. 4 Ternary diagrams for the chemical discrimination of micas. **a** $10*TiO_2 - (FeO + MnO) - MgO$ diagram for biotite after Nachit et al. (2005). Fields correspond to: (I) = magmatic, (II) = magmatic re-equilibrated, and (III) = secondary. **b** TiO_2–FeO–MgO diagram for muscovite after Monier et al. (1984). Fields correspond to: (I) = magmatic, (II) = late to post-magmatic, (III) = hydrothermal

constrained by subsolidus growth of Ms_2 with Si contents of 3.17 pfu and 35–36 mol.% of anorthite in Pl_2 (Figs. 7b and 8).

Monazite chemistry and dating

From a total of 54 chemical analyses on seven monazite grains in the deformed granite, 12 of them were discarded due to SiO_2 contents higher than 0.9 wt.% or total oxide sums lower than 96 wt.%. Selected chemical analyses and their corresponding calculated single ages are shown in Table 5. The monazite grains are 40–80 μm large and commonly display subidiomorphic to xenomorphic shapes in back-scattered electron (BSE) images (Fig. 10). They are usually enclosed in plagioclase, quartz, and K-feldspar, and more rarely in biotite, allanite, and apatite. Light and dark areas in BSE images reveal complex zonation patterns, mostly unrelated to crystal faces. Such zoning patterns are not correlated with a core-rim spatial distribution of ages determined on the monazite grains, as typical for other

complexly zoned monazite grains (*e.g.* Catlos 2013, and references therein).

The contents of the relevant oxides in wt.% (La_2O_3, UO_2, Y_2O_3, ThO_2, Nd_2O_3) of monazite versus their corresponding U–Th–Pb single ages (1σ-error) are shown in Fig. 11. The La_2O_3 contents range from 12.3 to 14.8 wt.% and show no correlation with the obtained ages (Fig. 11a). The contents of UO_2 (0.17–0.56 wt.%, Fig. 11b) and Y_2O_3 (0.11–2.17 wt.%, Fig. 11c) display a slight increase towards older ages. On the contrary, contents of ThO_2 (2.6–5.6 wt.%, Fig. 11d) and Nd_2O_3 (11.0–13.0 wt.%, Fig. 11e) slightly decrease towards these ages. A weighted mean age of 2092 ± 3 (2σ) Ma is obtained for all U-Th-Pb monazite ages without considering the single age of 1960 ± 19 (1σ), Ma which is statistically excluded by IsoplotR (Fig. 12a). Monazite yielding the cluster of ages between 2120 and 2045 Ma has a rather homogeneous composition, as shown in Fig. 11a–e, with some dispersion in La_2O_3 and ThO_2. This cluster is characterized by low Y_2O_3 contents mostly below 0.5 wt.%. Based on these chemical differences the U–Th–Pb ages cluster in two groups. Monazite of the older (I—four single ages) group is characterized by a weighted mean age of 2126 ± 10 (2σ) Ma (Fig. 12b). The group of thirty-seven analyses of chemically homogeneous monazite (II) yields a mean weighted age of 2089 ± 3.1 (2σ) Ma (Fig. 12b). The 95% confidence intervals, the mean square weighted deviations (MSWD), and chi-square *p*-values obtained for both groups are statistically acceptable and indicate the absence of overdispersion (Vermeesch 2018).

Discussion

Monazite U–Th–Pb ages and the Rhyacian to Orosirian geochronological framework of the Tandilia Belt

Monazite, an accessory mineral common in granitic and low-Ca metamorphic rocks (*e.g.* Montel 1993; Parrish 1990), has been increasingly used in geochronology for the past 30 years (Suzuki et al. 1991; Suzuki and Adachi 1991a, b; Montel et al. 1994). Similar to zircon, monazite might record inherited ages (*e.g.* Cocherie et al. 1998, 2005; Suzuki and Adachi 1991a), but as monazite is a refractory phase in peraluminous granitic melts due to the low solubility of phosphorous (e.g. Sawka et al. 1986), it is particularly useful in dating the studied rock. Piechocka et al. (2017) recently uttered this advantage of monazite over zircon in deciphering more precisely the crystallization ages of two Precambrian low-temperature leucocratic peraluminous magmatic supersuites of the Capricorn Orogen of SW Australia.

In situ U–Th–Pb dating of monazite grains of the studied peraluminous granite yields Paleoproterozoic, Rhyacian to
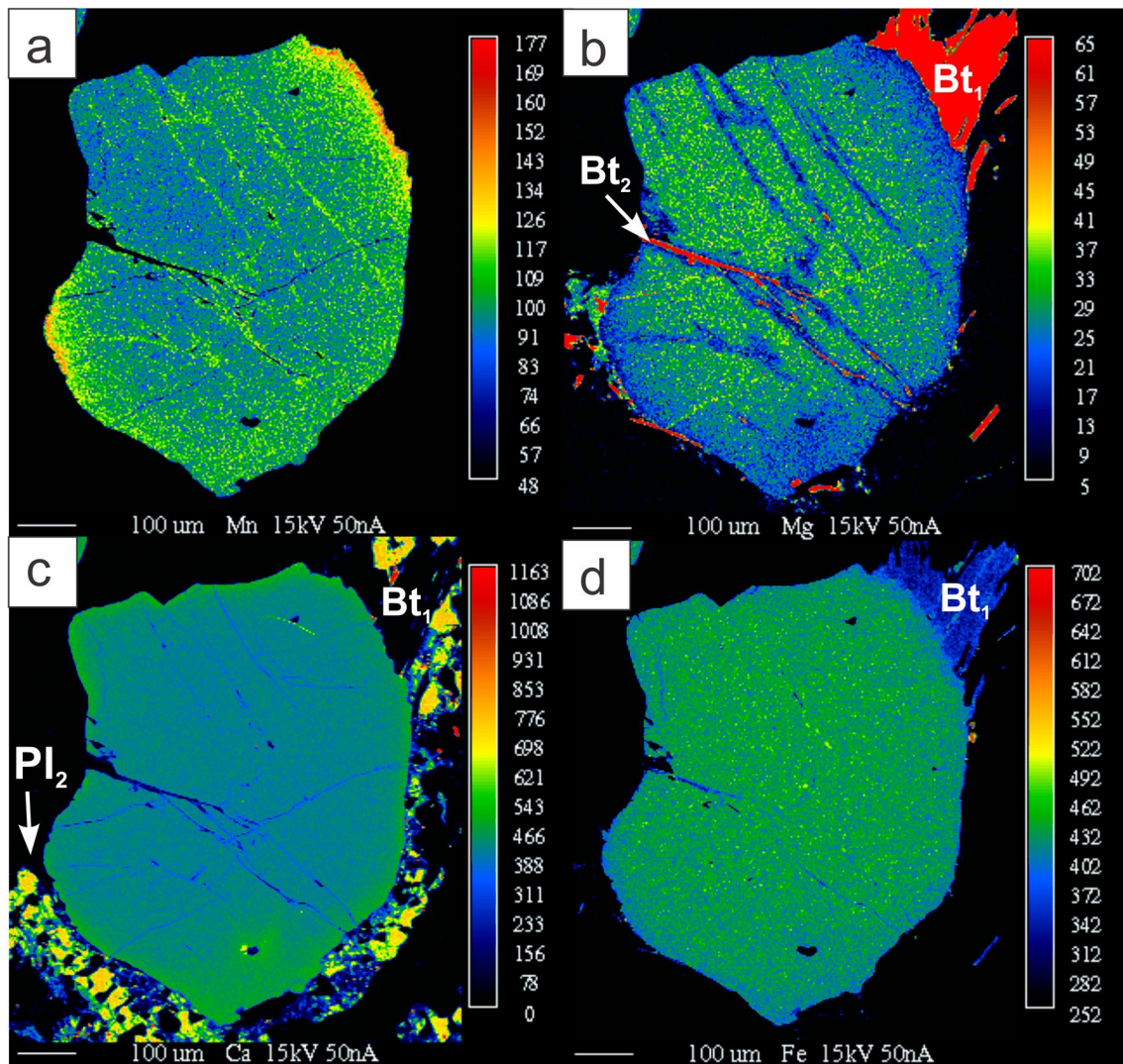
Fig. 5 Compositional maps obtained by X-ray scanning of garnet crystals in deformed granite LV0604. Bt_1 = igneous biotite; Bt_2 = secondary biotite; Pl_2 = fine-grained recrystallized plagioclase with myrmekitic texture

Orosirian, single ages from 2000 to 2160 Ma for the igneous-metamorphic main events, compatible with ages of the Trans-Amazonian (Almeida et al. 1973) or Transplatense (Santos et al. 2019) orogeny. The analyzed monazite yields two mean age clusters. The older mean weighted age of 2126 ± 10 (2σ) Ma (group I) is chemically characterized by relatively high contents of UO_2 and Y_2O_3 (Fig. 11). These chemical signatures are similar to monazite of migmatitic gneiss from La Plata hill for which a mean weighted age of 2127 ± 10 (2σ) Ma was determined by Bianchi et al. (2020). These authors attributed this monazite to a tectonothermal event prior to the anatexis of the metasedimentary protolith. Similar U–Th–Pb ages of 2140–2130 Ma were calculated for group I of monazites in migmatites from El Cristo–San Verán hills, but this group is geochemically characterized by low values (< 0.8 wt.%) of Y_2O_3 (Martínez et al. 2017),

unlike the oldest monazites of La Virgen hill. Recently, an upper concordia intercept age of 2130 ± 10 (2σ) Ma, obtained by LA-ICP-MS U–Th–Pb dating of zircon, was related to the crystallization of calc-alkaline rhyolitic dikes from El Quebracho hill in the TB (Martínez et al. 2020). Thus, the weighted average age of 2126 ± 10 Ma of monazite group I of La Virgen hill could be likely related to inherited ages of widespread magmatic and metamorphic events recorded in the TB. In summary, our group I age confirms an important crustal growth event also stated by other dating results obtained on zircon in rocks from the TB (*e.g.* Cingolani et al. 2002; Hartmann et al. 2002; Pankhurst et al. 2003) and other localities of the RPC by different dating techniques (*e.g.* Rapela et al. 2007; Santos et al. 2017). Granitoids and orthogneisses from the western TB (Olavarría area) yielded Sm–Nd isochrons of 2140 ± 88 and 2127 ± 68 Ma (excluding
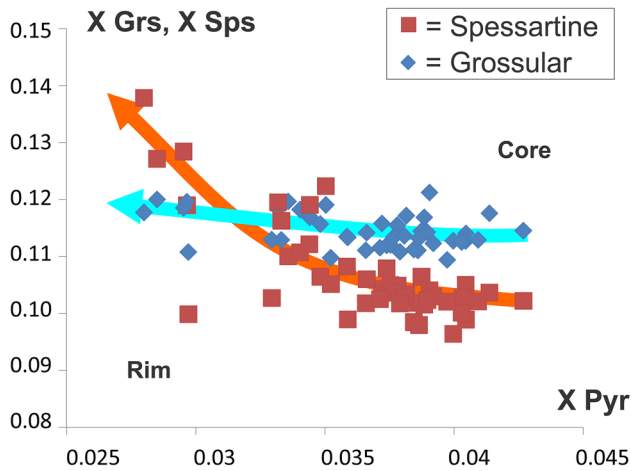
Fig. 6 Chemistry of garnet expressed as molar fractions of grossular (+ andradite) and spessartine versus that of pyrope in deformed granite LV0604. The solid arrows represent the chemical trends of spessartine (pink) and grossular (light blue) from core to rim

two enclaves from raw data). U–Pb SHRIMP ages, obtained on zircon from ten samples collected throughout the TB, point to a mean age of about 2150 Ma (Hartmann et al. 2002).

The main cluster of monazite (group II) with a weighted mean age of 2089 ± 3 (2σ) Ma can be linked to the crystallization of the garnet-bearing granite during a late to post-orogenic magmatic and metamorphic event which might include the anatexis of the country rocks. Our age also coincides with the 2088 ± 6 Ma determined by U–Pb SHRIMP dating on zircon from undeformed biotite monzogranite of the Ordoñez borehole at the western limit of the RPC, the Pampean Ranges of Córdoba (Rapela et al. 2007). Monazite from group II yielded commonly low Y_2O_3 values (< 0.5 wt. %). Considering the abundance of garnet in the studied deformed granite, we argue for the coexistence of garnet with the low-Y monazite group because Y distribution coefficients favor garnet as repository of Y and HREE (Pyle et al. 2001). Besides, the composition of garnet in the deformed granite is compatible with a magmatic origin, as detailed in the following section, implying that the group II weighted mean age should be related to the granite crystallization. Concerning similar low Y_2O_3 values, the group II age of monazite from El Cristo–San Verán migmatites is considerably younger (weighted mean age of 2012 ± 29 Ma), even younger than the proposed 'Camboriu' orogeny (Martínez et al. 2017). Monazite with low-Y and HREE contents yielding a weighted mean age of 2073 ± 23 (2σ) Ma was

Fig. 7 *P–T* pseudosection calculated for the simplified bulk-composition (Table 4) of garnet-bearing granite (LV0604) from La Virgen hill. Some tiny *P–T* fields are not labeled. *Am1* Ca-amphibole, *Am2* Ca-Na-amphibole, *And* andalusite, *Bt* biotite, *Cp* clinopyroxene, *Crd* cordierite, *Ep* epidote, *Gt* garnet, *Im* ilmenite, *L* melt, *Ms* muscovite, *Opx* orthopyroxene, *Rt* rutile, *Si* sillimanite, *Tt* titanite, *Us* magnetite-ulvöspinel, *V* H_2O
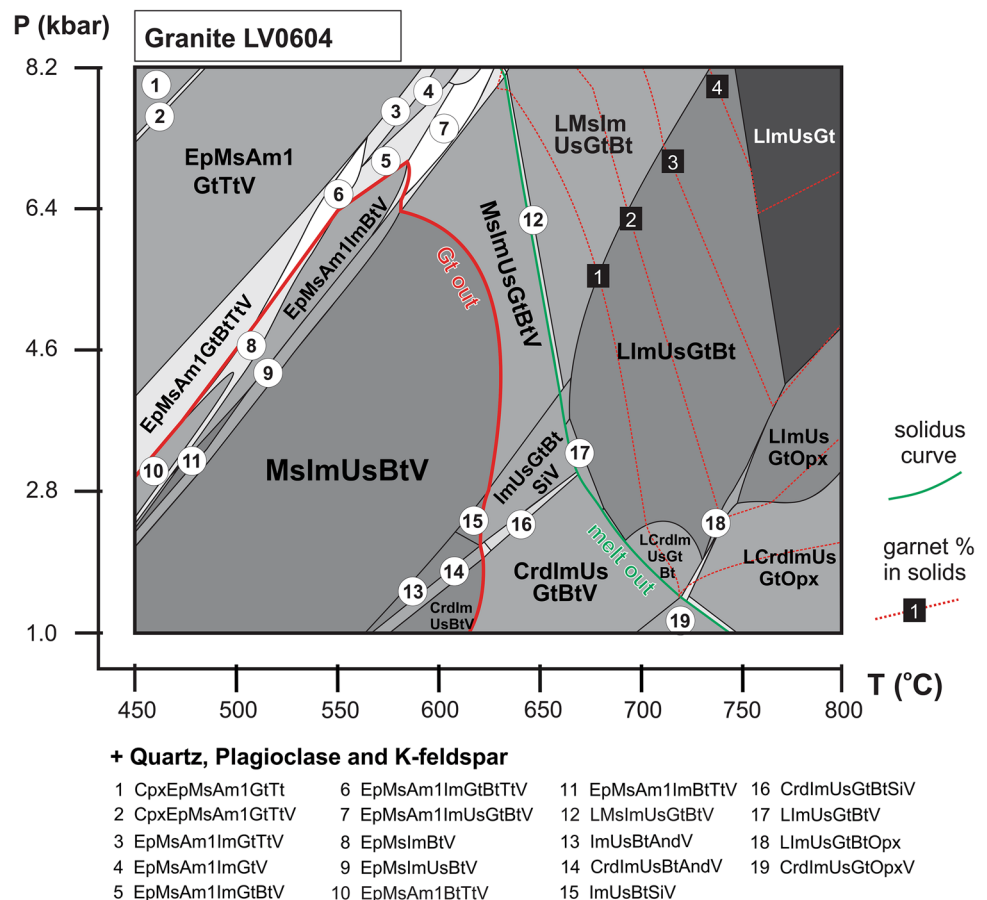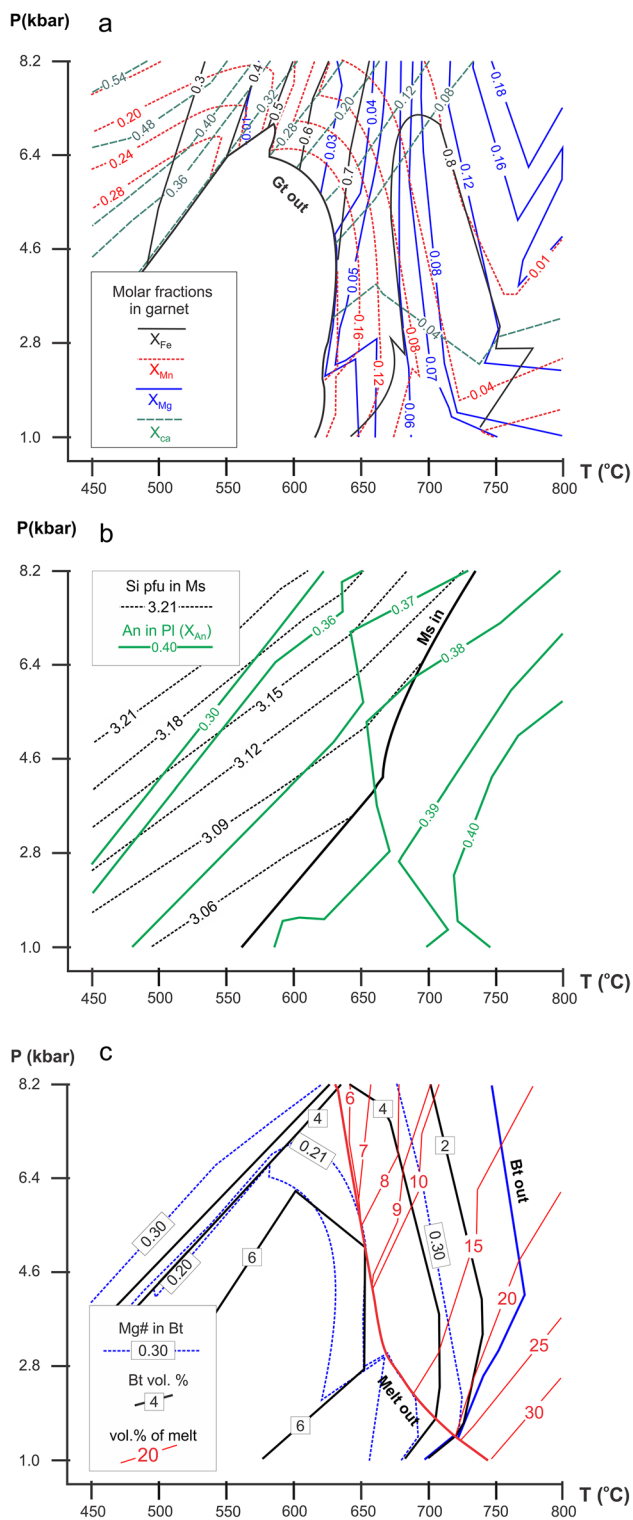
Fig. 8 Contouring of the *P–T* pseudosection of Fig. 7 by isopleths of different parameters of interest. **a** Isopleths for pyrope (X_{Mg}), spessartine (X_{Mn}), almandine (X_{Fe}), and grossular+andradite (X_{Ca}) components in garnet. **b** Isopleths for Si per formula unit in muscovite and anorthite molar content in plagioclase (X_{An}). **c** Calculated vol.% of melt and biotite and isopleths for Mg# in biotite

also reported from a metapelite of the Cinco Cerros area (Massonne et al. 2012). This age was interpreted to represent the age of an adjacent granite (Massonne et al. 2012). Therefore, a similar scenario is postulated to the intrusion of the deformed garnet-bearing granite of La Virgen hill although monazite ages for the migmatitic country rock were not determined yet. On the other hand, similar U–Pb crystallization ages were obtained from zircon of a granodiorite (2092 ± 13 Ma) and a gneiss with intermediate composition (2104 ± 7.6 Ma) exposed at the nearby Siempre Amigos hill. These ages were related to the 'Camboriu' orogeny (Angeletti et al. 2021).

The single age of 1960 ± 19 (1σ) Ma was discarded for the calculation of the group II weighted mean age according to the statistical criteria of IsoplotR (Vermeesch 2018). Nevertheless, monazite ages younger than 2000 Ma are common in the TB. In the area of Cinco Cerros hills, the youngest ages 1913 ± 11 (1σ) Ma and 1805 ± 21 (1σ) Ma were linked to deformation of the continental crust during the final exhumation and slow cooling of the orogen (Massonne et al. 2012). A similar interpretation was given for a single monazite age of 1975 ± 18 Ma in the migmatitic gneiss of La Plata hill (Bianchi et al. 2020).

Petrochronology: the deciphered *P–T–t–d* path

The studied pluton is one of many small intrusives (or peraluminous leucogranites) generated during the late collisional stage of the orogeny and widespread in the basement rocks of the TB. Thermodynamic modeling of similar intrusives, which are located at the southeastern part of the belt (Massonne et al. 2012; Martínez et al. 2017), is scarce. Therefore, the deciphered *P–T* path helps us to understand the geodynamic processes during the formation of the 'Camboriu' orogeny in the TB. Compositions of garnet in the studied peraluminous granite are identical to the common almandine-rich magmatic garnet (Dahlquist et al. 2007) with spessartine component above 10 mol.% (Miller and Stoddard 1981). The derived early *P–T* path is based on this magmatic garnet, the core ($pyr_4(grs + adr)_{11}sps_{10}alm_{75}$) crystallization of which constrains the emplacement conditions of La Virgen hill granite at mid-crustal depths of ~22 km and temperatures of around 650 °C (point A in Fig. 9a). Nevertheless, isopleths of 38 mol.% of anorthite in plagioclase (Pl_1) and muscovite with the higher TiO_2 contents (~0.5 wt.%) and the lowest Si contents (3.10 pfu) record a magmatic (Fig. 4b) crystallization at somewhat higher temperatures than point A (~700 °C) and similar pressures not fully constrained in Fig. 9b. This means that garnet grew after plagioclase and muscovite (Fig. 7) and is consistent with late crystallization of garnet in granite reported, for instance, by Massonne et al. (2004).
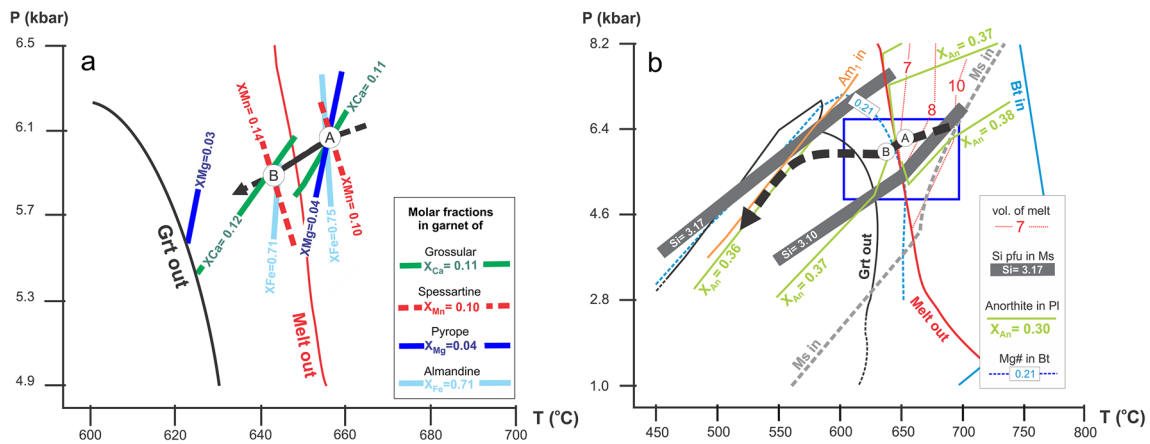
Fig. 9 *P–T* path determined for the studied deformed garnet-bearing granite based on the pseudosection shown in Figs. 7 and 8 represented by a thick, black dashed-line arrow. **a** Intersections of isopleths of molar components in the garnet core (point A) and rim (point B) in a magnified *P–T* range with respect to that of the pseudosection

shown in Figs. 7 and 8. **b** *P–T* paths constrained by points A–B (blue square corresponds to Fig. 8a), isopleths of anorthite (X_{An}) in plagioclase, Mg# in biotite, and Si (pfu) in muscovite. Abbreviations as in Fig. 7

Fig. 10 Back-scattered electron images of representative monazite grains from the deformed garnet-bearing granite LV0604 with marked spots at which the given ages were determined (ages in Ma, errors as 1σ). **a** Subhedral monazite crystal (Mnz 4) with embayments, fracture and complex internal compositional domains included in plagioclase. **b** Idiomorphic rounded monazite (Mnz 5) in plagioclase. **c** Subidioblastic large monazite with fractures (Mnz 6) in biotite and plagioclase. **d** Idiomorphic monazite (Mnz 7) in plagioclase with a large fracture and complex internal compositional domains included in plagioclase
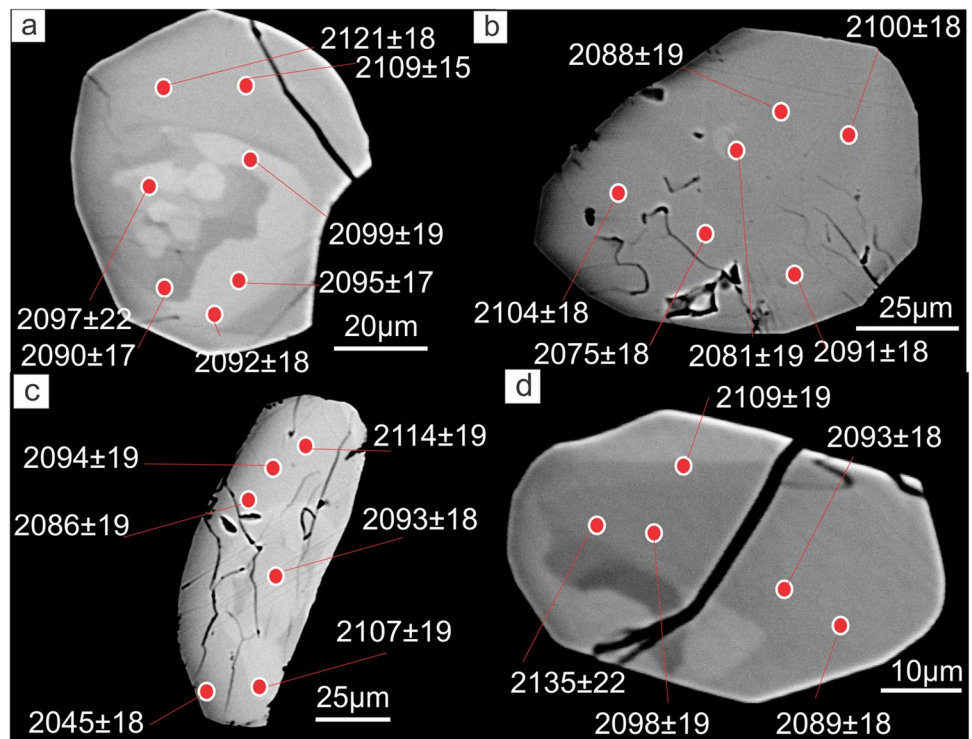
Cooling of garnet crystals at subsolidus conditions to point B (Fig. 8a) generated the slight rimward zoning (Fig. 5) with decreasing almandine content from 75 to 71 mol.% (X_{Fe} = 0.71) and increasing spessartine content from 10 to 14 mol.% (X_{Mn} = 0.14) possibly by slow cation interdiffusion involving MnO-poor magmatic biotite (< 0.1 wt.%). According to the calculation results (Fig. 8c), this biotite (Bt₁), which is more widespread (~ 7 vol.% observed, 6 vol. % calculated) than clustered garnet (max. 5 vol.%

observed, 0.4 vol.% calculated), chemically equilibrated (Mg# of 0.21) between points A and B in Fig. 9b. This equilibration towards point B is assumed to have been caused by a much faster Fe and Mg exchange in biotite than in garnet (Fernando et al. 2003). The low amount of pyrope in garnet and its slight decrease (Figs. 5b and 6) from core (4 mol.%: X_{Mg} = 0.04) to rim (< 3 mol.%) led to uncertainties in isopleth intersections to fix point B (Fig. 9a). Nevertheless, this point is well constrained by X_{Mn} and X_{Ca} in

Fig. 11 Contents of main oxides (wt.%) in monazite from the studied deformed garnet-bearing granite. From **a** to **e**, various oxide contents plotted *versus* U–Th–Pb ages (Ma). The shaded area that spreads between 2120 and 2140 Ma refers to monazite of the older group I
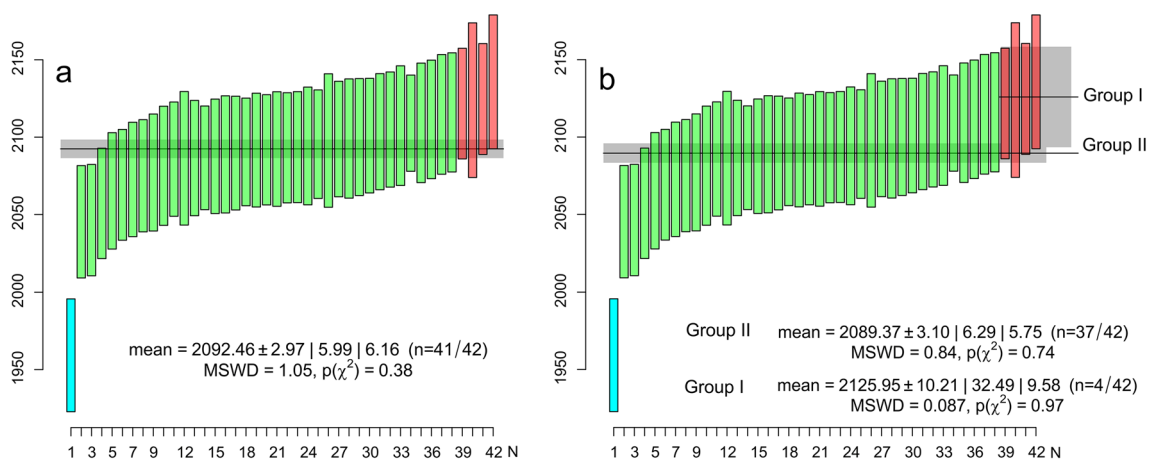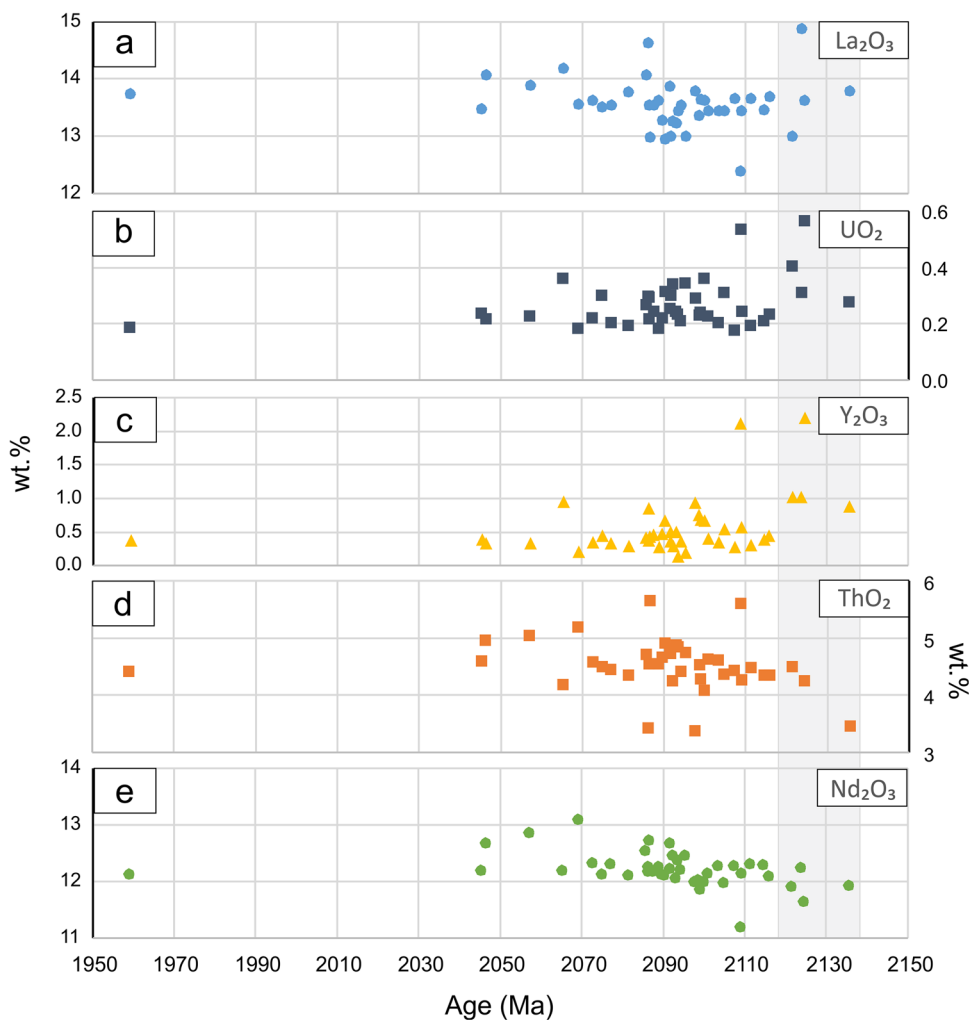

Fig. 12 Distribution of U–Th–Pb monazite single ages (error bar length is ±1σ) and calculation of weighted mean ages. **a** All monazite ages. **b** Ages of the three groups of monazite. The single age of 1960±19 Ma was statistically excluded (in light blue). Mean weighted ages in both diagrams are presented with their respective 95% confidence interval shaded in gray

garnet. As a result, the crystallization of the studied granite occurred at mid-crustal levels at ~ 2.08 Ga, possibly during the Rhyacian late- to post-tectonic stage of the Camboriu orogeny proposed by several authors (*e.g.* Cingolani et al. 2002; Hartmann et al. 2002; Chernicoff et al. 2015; Martínez et al. 2017; Oyhantçabal et al. 2018; Santos et al. 2019) or during the suggested underthrusting of oceanic crust (Massonne et al. 2012). Most of the exposed rocks in the TB (Buenos Aires Complex) are profuse granites (sensu lato) and high-grade migmatitic country rocks older than 2.0 Ga which denote paleodepths of 20–25 km (Massonne et al. 2012; Martínez et al. 2017; Bianchi et al. 2020; this work). The corresponding exhumation *P–T* paths for these late to post-collisional rocks are those of clockwise paths with cooling during exhumation, named type I in the introduction. Such exhumation might have occurred under normal to high geothermal gradients (45–50 °Ckm^{-1}), as stated for the areas of San Verán hill (Martínez et al. 2017) and La Plata hill (Bianchi et al. 2020).

Exhumation processes in orogens include thrusting, normal faulting, ductile thinning and erosion (Ring et al. 1999). The shape of the *P–T* path could deliver information on the dominant exhumation process (Gapais et al. 2009). For instance, orogens involving initially hot and weak lithosphere show retrograde *P–T* paths along geotherms, which may indicate that units remained close to thermal equilibrium with surrounding domains during decompression (Gapais et al. 2009). As strain is likely distributed in orogenic roots, potentially accommodated through dominant steeply dipping foliations without recognition of low-angle faults, erosion is likely the main exhumation process (Gapais et al. 2009). Also, steeply dipping foliations point to vertical stretching of material, which may be an effective exhumation process in the TB. If the latter is true, the present Moho depth in the TB at nearly 40 km (Kostadinoff 1995; Del Cogliano 2006) and the unroofing of 20–25 km thick supra-crustal orogenic material points to a Paleoproterozoic orogenic crust with a thickness of at least 60 km.

The post-magmatic formation of muscovite (Fig. 4b) at feldspar rims (Ms$_2$) with Si contents of up to 3.17 (pfu) and low TiO$_2$ contents constrains the initial exhumation path of the granite at La Virgen hill. The crystallization of this muscovite and the amphibole absence in the studied rock suggests isobaric cooling from point B to ~ 560 °C. Epidote, formed as replacement product of feldspars, appears in a narrow field during this isobaric cooling path (field 9, Fig. 7) probably as a consequence of local equilibria. The fine-grained recrystallized plagioclase (Pl$_2$) (Fig. 3e) with 35–36 mol.% of anorthite (andesine) points to deformation during exhumation of the granite. Microstructures of deformation such as myrmekite (Fig. 3a) and flame perthite might have formed at subsolidus conditions below 560 °C and 5 kbar (Passchier and Trouw 2005). The microstructure

of core and mantle in feldspar points to dislocation creep by subgrain rotation deformation at temperatures above 450 °C or more likely above 550 °C (Pryer 1993; Passchier and Trouw 2005). Myrmekite is a deformation-induced product of granitic mylonites developed at amphibolite-facies metamorphic conditions (*e.g.* Simpson and Wintsch 1989). Subgrain rotation and grain boundary migration recrystallization are common in quartz, and indicate temperatures of 400–500 ºC and 500–700 ºC, respectively (Stipp et al. 2002). Pervasive deformation is concentrated in subvertical mylonite belts with E-W strike. The AMSZ, located only 4 km south of La Virgen hill, is the most impressive crustal-scale deformation zone of the TB with a dominant pure-shear and minor transcurrent components (*e.g.* Frisicale et al. 1999). Conditions of deformation affecting the granitic rocks from the AMSZ were estimated by a microstructural analysis and thermodynamic modeling of mylonite bulk compositions above 400–450 °C and at pressures of more than ~ 6 kbar (Frisicale et al. 2005). These conditions are similar to those estimated for the deformation of the granite in the study area. Rocks deformed at deeper crustal conditions of 600–700 °C and 8.0–9.0 kbar are exposed in the Cerro Negro hill at the northwestern terminus of the AMSZ, where different stages of pseudotachylites, produced under ductile to brittle conditions, are accompanied by rapid exhumation, probably due to repeated seismic slip (Frisicale et al. 2012). Monazite ages and microstructures in the studied rocks constrain deformation processes at subsolidus conditions after 2.08 Ga. These processes are probably concomitant with exhumation processes at greenschist-facies metamorphic conditions at the youngest ages recorded at *ca.* 1.9 Ga. A further long-lasting slow exhumation might have occurred until the intrusion of basaltic tholeiitic dike swarms in cold rocks during an extensional tectonic regime at 1.6 Ga (Iacumin et al. 2001; Teixeira et al. 2002).

Conclusions

In our geothermobarometric study, a cooling and exhumation path was deciphered for the deformed garnet-bearing granite of La Virgen hill in the western TB. This path is complemented by observations of microstructures and U–Th–Pb dating of monazite. The age of a group of older monazite of 2126 ± 10 Ma is common for igneous-metamorphic events in the entire RPC. The crystallization of the studied peraluminous leucogranite at *P–T* conditions of 6.0 kbar and 655 °C occurred at 2089 ± 3 Ma and is recorded by the younger monazite group. The subsequent cooling path suggests a slow exhumation of mid-crustal rocks, of which the studied granite was part of, until ca. 1.9 Ga (the youngest monazite single age in this study). This cooling was concomitant with horizontal shortening and the development

of E–W striking mylonite belts under conditions of the low amphibolite to greenschist-facies metamorphism.

Declarations

Conflict of interest The authors declare that they have no known competing financial interests or personal relationships that could have appeared to influence the work reported in this paper.

References

Almeida FFM, Amaral G, Cordani UG, Kawashita K (1973) The Precambrian evolution of the South American cratonic margin, south of the Amazon River. In: Nairn AE, Stehli FG (eds) The ocean basins and margins I. Plenum Publishing, New York, pp 411–446

Angeletti M, Chichorro M, Frisicale MC, Castro A, Dimieri LV (2014) Nuevas edades radiométricas U-Pb SHRIMP en Tandilia, cerro Siempre Amigos, Sierras de Azul, Buenos Aires, Argentina. 19° Congreso Geológico Argentino, Córdoba. Sesión Temática Petrología Ignea y Metamórfica T8-01:2

Angeletti M, Frisicale MC, Dimieri LV (2016) Petrografía, caracterización geoquímica y análisis microestructural del granito del cerro Siempre Amigos, sierras de Azul. Tandilia Rev Asoc Geol Argentina 73(2):211–224

Angeletti M, Martinez JC, Frisicale MC (2017) Trayectoria de evolución metamórfica P-T-d del granito milonítico paleoproterozoico de Cerro Negro, megacizalla de Azul, Tandilia. Actas 20° Congreso Geológico Argentino, San Miguel de Tucumán 5:10–12

Angeletti M, Martínez JC, Frisicale MC, Massonne H-J (2019) P-T-d path of a garnet-bearing metagranite from the Paleoproterozoic basement of the Tandilia terrane, Rio de la Plata craton, Argentina. Latin-American Colloquium of Geosciences, Hamburg, Germany, pp 28–29

Angeletti M, Chichorro M, Castro A, Frisicale MC, Solá R, Dimieri LV (2021) New geochemical, U–Pb SIMS geochronology and Lu–Hf isotopic data in zircon from Tandilia basement rocks, Río de la Plata craton, Argentina: evidence of a sanukitoid precursor for some Paleoproterozoic granitoids. J S Am Earth Sci 108:103199. https://doi.org/10.1016/j.jsames.2021.103199

Bernhardt H-J (2007) MINCALC-V5, a software tool for mineral analyses data processing. Acta Microsc 16(Supp. 2):43–44

Bianchi FD, Martínez JC, Angeletti M, Frisicale MC, Massonne H-J, Dristas JA (2020) Paleoproterozoic P-T-d-t evolution of a gneiss with quartz-sillimanite nodules from the Azul ranges, Rio de la Plata craton, Argentina. J South Am Earth Sci. https://doi.org/10.1016/j.jsames.2019.102453

Brandelik A (2009) CALCMIN—an Excel^TM visual basic application for calculating mineral structural formulae fromelectron microprobe analyses. Comput Geosci 35:1540–1551

Catlos EJ (2013) Versatile Monazite: resolving geological records and solving challenges in materials science. Generalizations about monazite: implications for geochronologic studies. Am Miner 98:819–832

Chernicoff C, Zappettini EO, Peroni J (2014) The Rhyacian El Cortijo suture zone: aeromagnetic signature and insights for the geodynamic evolution of the southwestern Río de la Plata craton, Argentina. Geosci Front 5:43–52

Chernicoff CJ, Zappettini EO, Santos JO, Pesce A, McNaughton NJ (2015) Zircon and Titanite U-Pb SHRIMP dating of unexposed basement units of the Buenos Aires region, southeastern Río de La Plata Craton, Argentina. Int Geol Rev 58(5):643–652

Cingolani CA (2011) The Tandilia System of Argentina as a southern extension of the Río de la Plata craton: an overview. Int J Earth Sci (geol Rundsch) 100:221–242

Cingolani CA, Hartmann LA, Santos JOS, McNaughton NJ (2002) U-Pb SHRIMP 23 dating of zircons from the Buenos Aires complex of the Tandilia belt, Río de La Plata craton, Argentina. 15° Congreso Geológico Argentino 1:149–154 (**El Calafate, Santa Cruz**)

Cingolani CA, Santos JOS, McNaugthon NJ, Hartmann LA (2005) Geocronología U-Pb SHRIMP sobre circones del Granitoide Montecristo. Tandil, Provincia de Buenos Aires, Argentina. Actas 16º Congreso Geológico Argentino, La Plata 1:299–302

Cocherie A, Legendre O, Peucat J-J, Kouamelan AN (1998) Geochronology of polygenetic monazites constrained by in situ electron microprobe Th-U-total lead determination: implications for lead behavior in monazite. Geochim Cosmochim Acta 62:2475–2497

Cocherie A, Be Mézème E, Legendre O, Fanning CM, Faure M, Rossi P (2005) Electron microprobe dating as a tool for determining the closure of Th-U-Pb systems in migmatitic monazites. Am Miner 90:607–618

Connolly JAD (1990) Multivariate phase diagrams: an algorithm based on thermodynamics. Am J Sci 290:666–718

Connolly JAD (2005) Computation of phase equilibria by linear programming: a tool for geodynamic modeling and its application to subduction zone decarbonation. Earth Planet Sci Lett 236:524–541

Dahlquist JA, Galindo C, Pankhurst RJ, Rapela CW, Alasino PH, Saavedra J, Fanning CM (2007) Magmatic evolution of the Peñón

Rosado granite: petrogenesis of garnet-bearing granitoids. Lithos 95:177–207

Dale J, Holland T, Powell R (2000) Hornblende-garnet-plagioclase thermobarometry: a natural assemblage calibration of the thermodynamics of hornblende. Contrib Mineral Petrol 140(3):353–362

Dalla Salda L (1981) The Precambrian geology of El Cristo, southern Tandilia region, Argentina. Int J Earth Sci (geol Rundsch) 70:1030–1042

Dalla Salda LH, Spalletti LA, Poiré DG, De Barrio R, Echeveste H, Benialgo A (2006) Tandilia. Temas de Geología Argentina 1. Serie Correlación Geológica 21:17–46

Del Cogliano D (2006) Modelado del Geoide con GPS y Gravimetría. Caracterización de la Estructura Geológica de Tandil. Unpubl. Ph.D. thesis, Facultad de Ciencias Exactas, Ingeniería y Agrimensura, Universidad Nacional de Rosario, Rosario, Argentina

Delpino SH, Dristas JA (2008) Dolomitic marbles and associated calc-silicates, Tandilia belt, Argentina: geothermobarometry, metamorphic evolution, and P–T path. J S Am Earth Sci 25(4):501–525

Dristas JA (1983) Petrología de una metariolita en la Sierra del Tigre, Tandilia. Rev Asoc Geol Argentina 38(2):192–200

Dristas JA, Martínez JC, Massonne H-J, Pimentel MM (2013) Mineralogical and geochemical characterization of a rare ultramafic lamprophyre in the Tandilia Belt basement, Río de la Plata Craton, Argentina. J South Am Earth Sci 43:46–61

Fernando GWAR, Hauzenberger CA, Baumgartner LP, Hofmeister W (2003) Modeling of retrograde diffusion zoning in garnet: evidence for slow cooling of granulites from the Highland Complex of Sri Lanka. Miner Petrol 78:53–71. https://doi.org/10.1007/s00710-002-0224-1

Frisicale MC, Dimieri LV, Dristas JA (1999) Megacizalla en Boca de la Sierra, Tandilia: Convergencia normal? 14° Congreso Geológico Argentino, Salta 1:168–171

Frisicale MC, Martinez F, Dimieri LV, Dristas J (2005) Microstructural analysis and P-T conditions of the Azul megashear zone, Tandilia, Buenos Aires province, Argentina. J South Am Earth Sci 19:433–444

Frisicale MC, Dimieri LV, Dristas JA, Araujo VS, Fortunatti N (2012) Microstructural and geochemical analysis of Paleoproterozoic pseudotachylytes in Río de la Plata craton, Tandil belt, Argentina. Geol Acta 10:85–101

Fuhrman ML, Lindsley DH (1988) Ternary-feldspar modeling and thermometry. Am Miner 73:201–215

Gapais D, Cagnard F, Gueydan F, Barbey P, Ballèvre M (2009) Mountain building and exhumation processes through time: inferences from nature and models. Terra Nova 21:188–194. https://doi.org/10.1111/j.1365-3121.2009.00873.x

González Bonorino F, Zardini MA, Figueroa M, Limousin TA (1956) Estudio Geológico de las Sierras de Olavarría y Azul (Provincia de Buenos Aires). Laboratorio De Ensayo De Materiales e Investigaciones Tecnológicas, Serie 2(63):47–65 (**La Plata, Argentina**)

Hartmann LA, Santos JOS, Cingolani CA, McNaughton NJ (2002) Two Paleoproterozoic orogenies in the evolution of the Tandilia Belt, Buenos Aires, as evidenced by zircon U-Pb SHRIMP geochronology. Inter Geol Rev 44:528–543

Holland TJB, Powell R (1991) A compensated Redlich-Kwong equation for volumes and fugacities of CO_2 and H_2O in the range 1 bar to 50 kbar and 100–1600 °C. Contrib Miner Petrol 109:265–273

Holland TJB, Powell R (1998) An internally consistent thermodynamic data set for phases of petrological interest. J Metamorph Geol 16:309–343

Iacumin M, Piccirillo EM, Girardi VAV, Teixeira W, Bellieni G, Echeveste H, Fernández R, Pinese JPP, Ribot A (2001) Early Proterozoic calc-alkaline and middle Proterozoic tholeiitic dyke swarms from central-eastern Argentina: petrology, geochemistry, Sr–Nd isotopes and tectonic implications. J Petrol 42:2109–2143

Kostadinoff J (1995) Geofísica de las Sierras del Sistema de Tandil. Unpubl. Ph.D. thesis, Facultad de Ciencias Astronómicas y Geofisicas, Universidad Nacional de La Plata, Argentina

Lajoinie MF, Etcheverry RO, Lanfranchini ME, Cabana MC (2014) Geología, geoquímica y génesis de diques proterozoicos del área de San Miguel, Sierras Septentrionales de la Provincia de Buenos Aires. Rev Asoc Geol Argentina 71(3):404–415

Liu Y, Siebel W, Theye T, Massonne H-J (2011) Isotopic and structural constraints on the late Miocene to Pliocene evolution of the Namche Barwa area, eastern Himalayan syntaxis, SE Tibet. Gondwana Res 19:894–909

Marchese H, Di Paola E (1975) Reinterpretación estratigráfica de la perforación de Punta Mogotes I, Provincia de Buenos Aires. Rev Asoc Geol Argentina 30(1):44–52

Martínez JC, Massonne H-J, Dristas JA, Theye T, Graff AA (2016) Paleoproterozoic migmatitic gneisses from the Tandilia belt (Argentina), Río de la Plata craton, record cooling at deep crustal levels. J S Am Earth Sci 67:201–220

Martínez JC, Massonne H-J, Frisicale MC, Dristas JA (2017) Trans-Amazonian U-Th-Pb monazite ages and P-T-d exhumation paths of garnet-bearing leucogranite and migmatitic country rock of the southeastern Tandilia belt, Rio de la Plata craton in Argentina. Lithos 274–275:328–348

Martínez JC, Massonne H-J, Dristas JA, Opitz J, Angeletti M (2020) Paleoproterozoic metamorphosed calc-alkaline dikes of the southwestern Río de la Plata craton, Tandilia belt of Argentina, record a prograde high-pressure, medium- temperature evolution. J South Am Earth Sci. https://doi.org/10.1016/j.jsames.2020.102595

Massonne H-J (2010) Phase relations and dehydration behaviour of calcareous sediments at very-low to low grade metamorphic conditions. Period Mineral 79(2):21–43

Massonne H-J (2011) Pre-conference field trip: Erzgebirge (Ore Mountains), Germany and Czech Republic; German part of the Saxonian Erzgebirge. Geolines 23:29–59

Massonne H-J (2012) Formation of amphibole and clinozoicite-epidote in eclogite owing to fluid infiltration during exhumation in a subduction channel. J Petrol 53(10):1969–1998. https://doi.org/10.1093/petrology/egs040

Massonne H-J, Calderón M, Hervé F (2004) Magmatic muscovite and garnet in granites of the Southern Patagonian Batholith. Boll Geofis Teorica Appl 45(2 Supplement):121–125

Massonne H-J, Kennedy A, Nasdala L, Theye T (2007) Dating of zircon and monazite from diamondiferous quartzofeldspathic rocks of the Saxonian Erzgebirge. Mineral Mag 71:407–425

Massonne H-J, Dristas JA, Martínez JC (2012) Metamorphic evolution of the Río de la Plata Craton in the Cinco Cerros area, Buenos Aires Province, Argentina. J South Am Earth Sci 38:57–70

Massonne H-J, Cruciani G, Franceschelli M, Musumeci G (2018) Anti-clockwise pressure-temperature paths record Variscan upper-plate exhumation: example from micaschists of the Porto Vecchio region, Corsica. J Metamorph Geol 36:55–77

Miller CF, Stoddard EF (1981) The role of manganese in the paragenesis of magmatic garnet: an example from the old woman-piute range, California. J Geol 89(2):233–246. https://doi.org/10.1086/628582

Monier G, Mergoil-Danier J, Labernardière H (1984) Générations successives de muscovites et feldspaths potassiques dans les leucogranites du massif de Millevaches (Massif Central francais). Bull Minér 107(1):55–68

Montel J-M (1993) A model for monazite/melt equilibrium and application to the generation of granitic magmas. Chem Geol 110:127–146

Montel J-M, Veschambre M, Nicollet C (1994) Datation de la monazite à la microsonde électronique. Competes Rendus Acad Sci Paris Serie II 318:1489–1495

Nachit H, Ibhi A, Abia EH, Ohoud MB (2005) Discrimination between primary magmatic biotites, reequilibrated biotites and neoformed biotites. Comptes Rendus Geosci 337:1415–1420

Oyhantçabal P, Siegesmund S, Wemmer K (2011) The Rio de la Plata Craton: a review of units, boundaries, ages and isotopic signatures. Int J Earth Sci (geol Rundsch) 100:201–220

Oyhantçabal P, Cingolani C, Wemmer K, Siegesmund S (2018) The Rio de la Plata Craton of Argentina and Uruquay. In: Siegesmund S, Bassei MA, Oyhantcabal P, Oriolo S (eds) Geology of Southwest Gondwana. Springer Nature

Pamoukaghlian K, Gaucher C, Frei R, Poiré DG, Chemale F, Frei D, Will TM (2017) U-Pb age constraints for the La Tuna granite and Montevideo Formation (Paleoproterozoic, Uruguay): unravelling the structure of the Río de la Plata Craton. J South Am Earth Sci 79:443–458

Pankhurst RJ, Ramos A, Linares E (2003) Antiquity of the Río de la Plata craton in Tandilia, southern Buenos Aires Province, Argentina. J South Am Earth Sci 16:5–13

Parrish RR (1990) U-Pb dating of monazite and its application to geological problems. Can J Earth Sci 27:1431–1450

Passchier CW, Trouw RAJ (2005) Microtectonics. Springer, Berlin

Piechocka AM, Gregory CJ, Zi J-W, Sheppard S, Wingate MTD, Rasmussen B (2017) Monazite trumps zircon: applying SHRIMP U-Pb geochronology to systematically evaluate emplacement ages of leucocratic, low-temperature granites in a complex Precambrian orogen. Contrib Miner Petrol 172:63. https://doi.org/10.1007/s00410-017-1386-5

Poiré DG, Spalletti LA (2005) La cubierta sedimentaria Precámbrica-Paleozoica inferior del Sistema de Tandilia. In: Barrio RE, Etcheverry RO, Caballé MF, Llambías E (eds) Geología y Recursos Minerales de la Provincia de Buenos Aires. 16° Congreso Geológico Argentino, Relatorio 4, La Plata, pp 51–68

Powell R, Holland TJB (1999) Relating formulations of the thermodynamics of mineral solid solutions; activity modeling of pyroxenes, amphiboles, and micas. Am Mineral 84(1–2):1–14

Pryer L (1993) Microstructures in feldspars from a major crustal thrust zone: the Grenville Front, Ontario, Canada. J Struct Geol 15:21–36

Pyle J, Spear F, Rudnick R (2001) Monazite-xenotime-garnet equilibrium in metapelites and a new monazite-garnet thermometer. J Petrol 42(11):2083–2107

Ramos VA (1999) Rasgos estructurales del territorio Argentino 1. Evolución tectónica del territorio argentino. In: Caminos R (ed) Geología Argentina, Anales SEGEMAR 29, Buenos Aires, vol 24, pp 715–784

Ramos VA, Leguizamón MA, Kay SM, Teruggi M (1990) Evolución tectónica de Las Sierras de Tandil (Provincia de Buenos Aires). Actas 11° Congreso Geológico Argentino, San Juan, Actas II:357–360

Rapalini AE, Sánchez Bettucci L, Badgen E, Vásquez CA (2015) Paleomagnetic study on mid-Paleoproterozoic rocks from the Rio de la Plata craton: implications for Atlantica. Gondwana Res 27:1534–1549

Rapela CW, Pankhurst RJ, Casquet C, Fanning CM, Baldo EG, González-Casado JM, Galindo C, Dahlquist J (2007) The Río de la Plata Craton and the assembly of SW Gondwana. Earth Sci Rev 83:49–82

Rapela CW, Fanning M, Casquet C, Pankhurst RJ, Spalletti L, Poiré DG, Baldo EG (2011) The Río de la Plata Craton and the adjoining Pan-African/Brasiliano terranes: their origins and incorporation into south-west Gondwana. Gondwana Res 20:673–690

Reed SJB, Buckley A (1998) Rare-earth element determination in minerals by electron probe microanalysis: application of spectrum synthesis. Miner Mag 62:1–8

Ring U, Brandon M, Willett S, Lister G (1999) Exhumation processes. Geol Soc London Spec Publ 154(1):1–27. https://doi.org/10.1144/GSL.SP.1999.154.01.01

Rogers JJW (1996) A history of continents in the past three billion years. J Geol 104:91–107

Santos JOS, Chernicoff CJ, Zappettini EO, McNauhton NJ, Greau Y (2017) U-Pb geochronology of Martin García, Sola, and Dos Hermanas Islands (Argentina and Uruguay): unveiling Rhyacian, Statherian, Ectasian, and Stenian of a forgotten area of the Río de la Plata Craton. J South Am Earth Sci 80:207–228

Santos JOS, Chernicoff CJ, Zappettini EO, McNaughton NJ, Hartmann LA (2019) Large geographic and temporal extensions of the Rio de la Plata Craton, South America, and its metacratonic eastern margin. Int Geol Rev 61:56–85

Sawka W, Banfield JF, Chappell BW (1986) A weathering-related origin of widespread monazite in S-type granites. Geochim Cosmochim Acta 50(1):171–175

Simpson C, Wintsch RP (1989) Evidence for deformation-induced K-feldspar replacement by myrmekite. J Metamorph Geol 7:261–275. https://doi.org/10.1111/j.1525-1314.1989.tb00588.x

Stipp M, Stütnitz H, Heilbronner R, Schmid S (2002) The eastern Tonale fault zone: a "natural laboratory" for crystal plastic deformation of quartz over a temperature range from 250 to 700 °C. J Struct Geol 24:1861–1884

Suzuki K, Adachi M (1991a) The chemical Th-U-total Pb isochron ages of zircon and monazite from the gray granite of the Hida Terrane, Japan. J Earth Planet Sci Nagoya Univ 38:11–37

Suzuki K, Adachi M (1991b) Precambrian provenance and Silurian metamorphism of the Tsunosawa paragneiss in the South Kitakami terrane, Northeast Japan, revealed by the chemical Th-U-total Pb isochron ages of monazite, zircon and xenotime. Geochem J 25:357–376

Suzuki K, Adachi M, Tanaka T (1991) Middle Precambrian provenance of Jurassic sandstone in the Mino Terrane, central Japan: Th-U-total Pb evidence from an electron microprobe monazite study. Sediment Geol 75:141–147

Teixeira W, Pinese J, Iacumin M, Girardi V, Piccirillo E, Echeveste H, Ribot A, Fernandez R, Renne P, Heaman L (2002) Calc-alkaline and tholeiitic dyke swarms of Tandilia, Rio de la Plata craton, Argentina: U-Pb, Sm-Nd and Rb-Sr ^{40}Ar-^{39}Ar data provide new clues for intraplate rifting shortly after Transamazonian orogeny. Precambrian Res 119:329–353. https://doi.org/10.1016/S0301-9268(02)00128-6

Teixeira W, D'Agrella-Filho MS, Hamilton MA, Ernst RE, Girardi VAV, Mazzucchelli M, Bettencourt JS (2013) U-Pb (ID-TIMS) baddeleyite ages and paleomagnetism of 1.79 and 1.59 Ga tholeiitic dyke swarms, and position of the Rio de la Plata craton within the Columbia supercontinent. Lithos 174:157–174

Teruggi ME, Kilmurray J, Dalla Salda L (1974) Los dominios tectónicos de la región de Balcarce. Rev Asoc Geol Argentina 29(3):265–276

Teruggi ME, Leguizamón M, Ramos V (1988) Metamorfitas de bajo grado con afinidades oceánicas en el basamento de Tandil: Implicaciones geotectónicas, provincia de Buenos Aires. Rev Asoc Geol Argentina 43(3):366–374

Vermeesch P (2018) IsoplotR: a free and open toolbox for geochronology. Geosci Front 9(5):1479–1493

White RW, Powell R, Holland TJB, Worley BA (2000) The effect of TiO_2 and Fe_2O_3 on metapelitic assemblages at greenschist and amphibolite facies conditions: mineral equilibria calculations in the system: K_2O–FeO–MgO–Al_2O_3–SiO_2–H_2O–TiO_2–Fe_2O_3. J Metamorph Geol 18:497–511

White RW, Powell R, Clarke GL (2003) Prograde metamorphic assemblage evolution during partial melting of metasedimentary rocks at low pressures: migmatites from Mt Stafford, Central Australia. J Petrol 44:1937–1960